eTransportation 11 (2022) 100152

Contents lists available at ScienceDirect

eTransportation

journal homepage: www.journals.elsevier.com/etransportation

Recent progress and perspectives on designing high-performance thick electrodes for all-solid-state lithium batteries

Xiaofei Yang, Kieran Doyle-Davis, Xuejie Gao, Xueliang Sun*

Department of Mechanical and Materials Engineering, University of Western Ontario, London, Ontario, N6A 5B9, Canada

ARTICLE INFO

Article history:
Received 22 June 2021
Received in revised form
20 November 2021
Accepted 15 December 2021
Available online 17 December 2021

Keywords:
Thick electrode
Solid-state batteries
High-energy-density
Lithium metal batteries
Safety

ABSTRACT

All-solid-state lithium batteries (ASSLBs) with higher energy density and improved safety have been regarded as an alternative to the state-of-the-art Li-ion batteries. As a critical component of the battery, the active materials are stored in the cathode, which directly determines the capacity and energy density output. Increasing the thickness of the electrodes can raise the ratio of active materials in the packaged cell, thus showing the potential to achieve higher energy densities. However, the development of thickness-based ASSLBs is still hindered by the sluggish electrochemical kinetics caused by the slow Li^+/e^- transport in the high-tortuosity channels/pathways. In this review, we comprehensively summarize the recent progress in the emerging area of thick electrodes to solve the critical issue and develop high-performance ASSLBs. Firstly, we overview the recent developments in the design of thick electrodes with continuous Li^+/e^- transport pathways and low-tortuosity structures. After that, the interfacial engineering on creating a favorable SSE/electrode material interface is reviewed. Subsequently, several factors such as particle size, binder, crystal structure and solvent that have a great influence on building Li^+/e^- transport pathways are discussed. Moreover, the improvement of intrinsic electrochemical kinetics via high-conductivity electrode design is introduced. Lastly, the recent development of thick electrode-based ASSLB pouch cells are summarized, and the future directions of thick electrodes in ASSLBs are speculated upon.

1. Introduction

Aided by 30 years of development, Li-ion batteries based on intercalation/de-intercalation chemistry have been widely applied in portable electronic devices with reliable energy density over 200 Wh kg^{-1} [1,2]. However, the use of graphite anodes in the liquid electrolyte hindered their further improvement in energy density (eg. >300 Wh kg^{-1}) to meet the increasing global requirements for long-range electric vehicles (EVs) [3,4]. One of the most promising strategies to achieve higher energy density is replacing the widely used graphite anode (372 mAh g^{-1}) with Li metal anode (3860 mAh g^{-1}), while addressing the safety concerns induced by Li metal anode with the introduction of non-flammable solid-state electrolytes (SSEs) [3,5–9]. Recently, tremendous efforts have been focused on synthesizing high-ionic-conductivity and high chemical/electrochemical stability SSEs and addressing the SSE/electrode interfacial issues, and thus far great progress has been made [10–12]. For instance, sulfide superionic conductors as $Li_{10}GeP_2S_{12}$ (LGPS) and $Li_{9.54}Si_{1.74}P_{1.44}S_{11.7}Cl_{0.3}$ (LSPSCl) delivered extremely high room-temperature (RT) ionic conductivities of over 10^{-2} S cm^{-1} [13,14]. $Li_7La_3Zr_2O_{12}$ (LLZO) has an extremely high oxidization stability window over 5 V, while Li_3InCl_6 has demonstrated its scalable production, high air-stability, and chemical stability against oxidization below 4.2 V [15,16]. Based on the optimization of the battery structure and interfacial design, the assembled all-solid-state lithium batteries (ASSLBs) have demonstrated excellent cycling stability (>500 cycles) and rate performance (>2C) [17–22]. Besides, the companies of Samsung and OXIS Energy have recently accelerated their research and development toward industry-reliable ASSLBs [23,24]. As confirmed by OXIS Energy, they have successfully tested their lithium-sulfur (Li–S) battery cell prototypes at 471 Wh kg^{-1}, which can be expected to be further extended towards 600 Wh kg^{-1} with a significantly extended life cycle based on the solid-state Li–S technology. All these results suggest that the ASSLBs assembled with SSEs are promising directions to substitute state-of-the-art Li-ion batteries with improved energy density and safety.

* Corresponding author.
E-mail address: xsun9@uwo.ca (X. Sun).

https://doi.org/10.1016/j.etran.2021.100152
2590-1168/

As the critical component, the active materials stored in the electrode directly determine the capacity and energy density output. In other words, how to realize a high proportion of active materials (or electrode materials) in the total packaged cell mass is of the utmost importance [25,26]. Generally, the active materials (or electrode materials) ratio can be easily adjusted by changing the thickness of the electrode. If controlling for the same discharge capacity and voltage output, a thicker electrode always means a higher ratio of active materials (or electrode materials) in the packaged cell and a subsequent higher energy density output. Additionally, the thickness of the SSEs, especially for ceramic SSEs with high density, also has a great impact on the practical energy density. Fig. 1A illustrates the energy density and battery component ratios simulation based on the method proposed by Li's group [27]. Here LGPS is chosen as the representative SSE, while $LiNi_{0.8}Mn_{0.1}Co_{0.1}O_2$ (NMC-811) is chosen as the representative active material with a discharge capacity of 210 mAh g^{-1} and a discharge voltage of 3.8 V. The active materials content is controlled as 85 wt% and the negative electrode (Li) capacity/positive electrode capacity ratio (N/P) is controlled as 2. The thicknesses of the cathode current collector (Al) and anode current collector (Cu) are set as 16 μm and 8 μm, respectively. The SSE thickness is set as 20 μm to meet the requirements of practical application. As can be seen, at the current research state, where the active material loading is roughly 5 mg cm^{-2}, the weight ratio of electrode material (including inactive materials in the electrode) is 26 wt%-. Due to the extremely low cathode material ratio in the packaged cell, a relatively low practical energy density of 178 Wh kg^{-1} is expected to be achieved. Further raising the active material loading to 10 mg cm^{-2}, the ratio of the cathode material is increased to 41 wt% and the energy density is increased to 275 Wh kg^{-1}. If we control the active material loading up to 20 mg cm^{-2} (close to the value in the state-of-the-art liquid-electrolyte-based Li-ion batteries), a high cathode material ratio of 56 wt% can be achieved. Under these conditions, a high energy density of 378 Wh kg^{-1} is expected to be obtained, which can meet the energy density requirements of long-range EVs. In this regard, how to realize the combination of thick electrodes with thin SSEs is of significance to achieve high practical energy density over 300 Wh kg^{-1} [25]. The synthesis methods and application of thin SSEs in different ASSLB systems have been well-reviewed by previous review papers [28,29]. Herein, we will focus discussion on the design of high-performance thick electrodes.

As we mentioned above, raising the thickness of the cathode has the potential to increase the active material ratio and energy density output. Nevertheless, it is under the assumption that increasing the thickness of the electrode has a negligible effect on the capacity and voltage output. In actual application, thicker electrodes have several challenges that need to be overcome to maintain high capacity and voltage output. As illustrated in Fig. 1B, in conventional electrode configurations, where the cathode materials are slurry coated on Al current collector, increasing the electrode thickness will cause cathode cracking and cathode material shedding during the drying process. Moreover, with the increasing of electrode thickness, the transport distance of Li^+/e^- is prolonged (due to the high tortuosity of Li^+/e^- transport channels), resulting in poor charge transfer kinetics, large internal resistance and poor rate performance. On the other hand, compared with liquid-electrolyte systems, where liquid electrolyte forms continuous Li^+ transport pathway, the SSEs (especially for the ceramic particles) can hardly build continuous Li^+/e^- transport pathways via solid-solid contact. The discontinuous Li^+ transport pathways contribute to the low utilization of active materials and low capacity output [30].

Herein, we focus on reviewing recent progress in the emerging area of the structural design of thick electrodes to address the aforementioned issues and develop high-performance ASSLBs. Firstly, we overview the recent developments in the design of thick electrodes with continuous Li^+/e^- transport pathways and low-tortuosity structural design in different SSE systems. Afterward, the interfacial engineering on creating a favorable SSE/electrode material interface is reviewed. Subsequently, several physical and chemical factors (eg. particle size, binder, crystal structure and solvent) that have a great influence on building Li^+/e^- transport pathways are discussed. Moreover, the improvement of intrinsic electrochemical kinetics via high-conductivity electrode design is introduced. Additionally, the recent development of ASSLB pouch cells assembled with sheet-type thick electrodes is also summarized. Finally, we provide an outlook on the future directions of thick electrodes design and offer a promising roadmap toward higher energy density ASSLBs.

2. Thick electrode design

It is well known that the electrochemical performance can only occur at the tri-phase interface of active materials, Li^+ conductor and e^- conductor. Given the different transfer pathways of Li^+ and e^- within the electrode, the electronic network can be built by the electrically conductive additives, while the ion transfer path can be

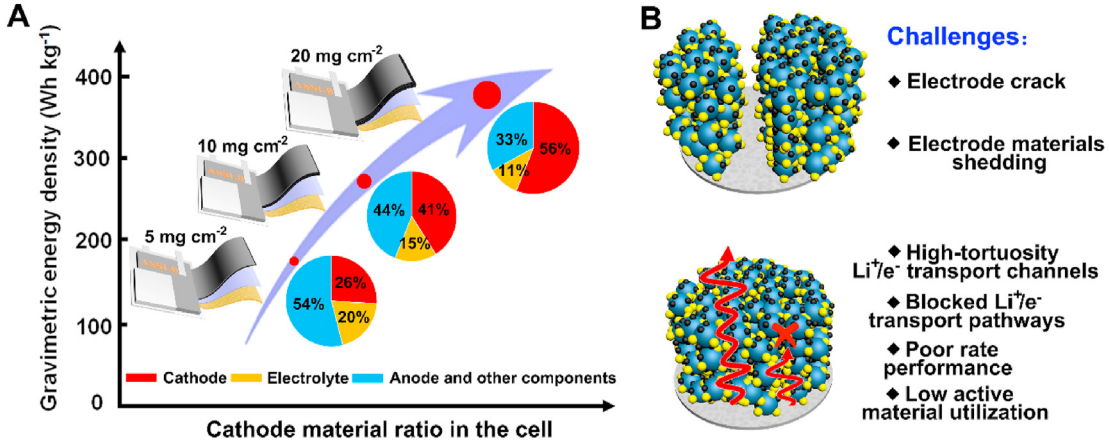

Fig. 1. Schematic view of the opportunities and challenges in the field of thick electrodes in ASSLBs. A) Evolution of energy density and battery component ratios from thick electrolyte/thin cathode to thin electrolyte/thick cathode. B) challenges accompanying the thick electrode design in ASSLBs.

formed by the continuous SSE phase among the active materials and electronic conductors. Compared with the construction of interconnected Li^+ transfer pathways, building an electronic network is much easier. The electronic conductivity of the electrode can be easily improved by raising the content of electrically conductive additives or introducing advanced 1D or 2D materials (eg. Carbon nanotubes, graphene) to change the electron transport model from "point-to-point" to "line-to-line" and "plan-to-plan". Herein, we will only discuss the influence of intrinsic electronic conductivity improvement of cathode materials and attention should be taken to choosing suitable electronic conductors. Most of the discussion will be focused on fabricating interconnected Li^+ transport pathways to accelerate Li^+ transport in the thick electrodes. It includes three parts. 1) designing continuous Li^+/e^- transport pathways and low-tortuosity structural design; 2) Interfacial engineering; 3) the influence of several physical and chemical factors, including the particle size, crystal structure, and solvent and binder effects. At the end of this section, Additionally, some recently reported ASSLB pouch cells assembled with sheet-type thick electrodes will be summarized. Recently reported thick electrodes and their performance are listed in Table 1.

2.1. Solid polymer electrolyte systems

Among various SSEs, solid polymer electrolytes (SPEs) show semi-liquid properties with higher flowability under high temperatures. The continuous Li^+ transport pathway configuration is much easier. In most cases, the conventional electrodes (no Li^+ conductor) used in the liquid electrolyte can be directly transferred into SPE-based ASSLBs, where SPEs diffuse into the pores to facilitate Li^+ transport. It should be noted that this strategy can only work under the premise of thin electrodes. The thin electrode is able to be well wetted by SPEs to make sure fast Li^+ transport and high capacity output. The situation will be completely different in thick electrodes. On one hand, it is very hard to guarantee the thick electrodes are completely wetted by the SPEs from top to bottom. In most cases, the SPEs can only wet the top electrode materials, while the bottom electrode materials are left dry and lacking Li^+ transport pathways, thus resulting in low active material utilization, large overpotential and poor rate performance. On the other hand, a large amount of electrolyte loss from SPEs will lead to reduced electrolyte thickness or electrolyte perforation, attributed to shortened battery cycling life or the occurrence of a short circuit.

To address the aforementioned issues, a common strategy is introducing SPEs during electrode fabrication. The SPE in the electrodes plays two roles: 1) working as a binder to bind the electrode materials; 2) building Li^+ transport pathways to facilitate Li^+ transport. Fan et al. investigated the difference in electrochemical performance with and without Li^+ conductors in the thick cathodes. As shown in Fig. 2A and B, with the Li^+ conductor (succinonitrile (SCN) + bis(trifluoromethane)sulfonimide (LiTFSI)), the Li—$LiNi_{0.5}Mn_{0.3}Co_{0.2}O_2$ (NMC532) with 10.5 mg cm^{-2} NMC532 loading exhibited a lower overpotential and a higher discharge capacity (146.9 mAh g^{-1}) compared with its counterpart without the Li^+ conductor (131.7 mAh g^{-1}) at 0.1C. The improved electrochemical performance can be attributed to the increased Li^+ transport channels with the introduction of SCN+LiTFSI. Moreover, benefitting from the rational structure design, the ASSLBs presented excellent cycling stability within high capacity retention of 86.9% after 150 cycles [31]. In another study with a similar strategy (PEO + SCN + LiTFSI as the Li^+ conductor), Cui's group demonstrated a 2.1 mAh cm^{-2} Li—$LiFePO_4$ (LFP) ASSLB with a 13.6 mg cm^{-2} LFP-loaded cathode at 0.2 mA cm^{-2} (operating temperature: 55 °C). It should be noted that the silica aerogel reinforced composite polymer electrolyte used in this work is a thickness adjustable electrolyte. The thickness can be easily controlled in the range of 30 μm—500 μm, which has the potential to improve the practical energy density through a combination of thin electrolytes and thick electrodes [32].

In-situ polymerization of small molecular monomers is another good strategy to configure continuous Li^+ transport pathways in the thick electrode as well as reduce the interfacial resistance between electrode and electrolytes [33,53]. Before polymerization, the precursors (liquid state) are firstly injected into the battery.

Table 1
Summary of thick electrode-based SSLBs.

Cathode material	Thickness (μm)	Active material loading (mg cm^{-2})	Electrolyte	Operating temperature	Operating current density	Initial capacity (mAh g^{-1})	Cycle number	Capacity retention	References
NMC532	_	10.5	LLZO/PVDF-HFP	25	0.1C	147	150	86.9%	[31]
LFP	_	13.6	PEO/SiO_2/SCN	55	0.2 mA cm^{-2}	154	13	~95%	[32]
LFP	–	5	polyDOL	RT	1C	~90	700	~80%	[33]
LFP	–	10.5	PEO	80	0.1C	145	50	88%	[34]
S	70	7.5	LLZCN	–	0.2 mA cm^{-2}	645	32	~80%	[35]
S	200	10.8	LLZCN	60	0.1C	1250	40	80%	[36]
NMC811	200	13.1	LATP	60	0.1C	153	50	70%	[37]
NMC622	1000	15.7	LLZO	–	0.3 mA cm^{-2}	175	90	72%	[38]
S	50	5.4	LLZCN	RT	50 mA g^{-1}	1200	50	~92%	[39]
S	70	5.3	LLZO	RT	0.22 mA cm^{-2}	1244	8	~90%	[40]
NMC622	130	4–5	LLZO	RT	0.1C	125–135	–	–	[41]
LTO	81	9.3	LLTO	60	12 mA g^{-1}	170	–	–	[42]
S	–	3.6	LPSCl	RT	50 mA g^{-1}	830	60	~96	[43]
NMC622	–	17	LPSCl	90	0.05C	136	–	–	[44]
NMC622	–	~8.2	$Li_6PS_5Cl_{0.5}Br_{0.5}$	30	0.1C	146	100	~85%	[45]
LCO	–	48.7	Li_3InCl_6	RT	0.13 mA cm^{-2}	123	–	–	[46]
NMC111	74	16.3	$75Li_2S{\cdot}25P_2S_5$	RT	0.15 C	149	175	84%	[47]
NMC622	88	21	LiPSCl	30	0.025 C	112	13	~90%	[48]
$LiNi_{0.9}Mn_{0.05}Co_{0.5}O_2$	86	–	LiPSCl	RT	0.7 mA cm^{-2}	125	100	94%	[49]
$LiNi_{0.9}Mn_{0.05}Co_{0.5}O_2$	86	~41	LiPSCl	60	0.5C	146	1000	89%	[23]
SeS_2	–	15.3	Li_3PS_4/LGPS	60	30 mA g^{-1}	824	10	94%	[50]
LFP	92	–	polyether-based SPE	70	C/3	160	1400	~80%	[18]
NMC111	~60	9.5	$75Li_2S{\cdot}25P_2S_5$	30	0.064 mA cm^{-2}	114	–	–	[51]
$LiNi_{0.8}Co_{0.15}Al_{0.05}O_2$	250	35	$80Li_2S{\cdot}20P_2S_5$	25	0.1C	110	100	82%	[52]

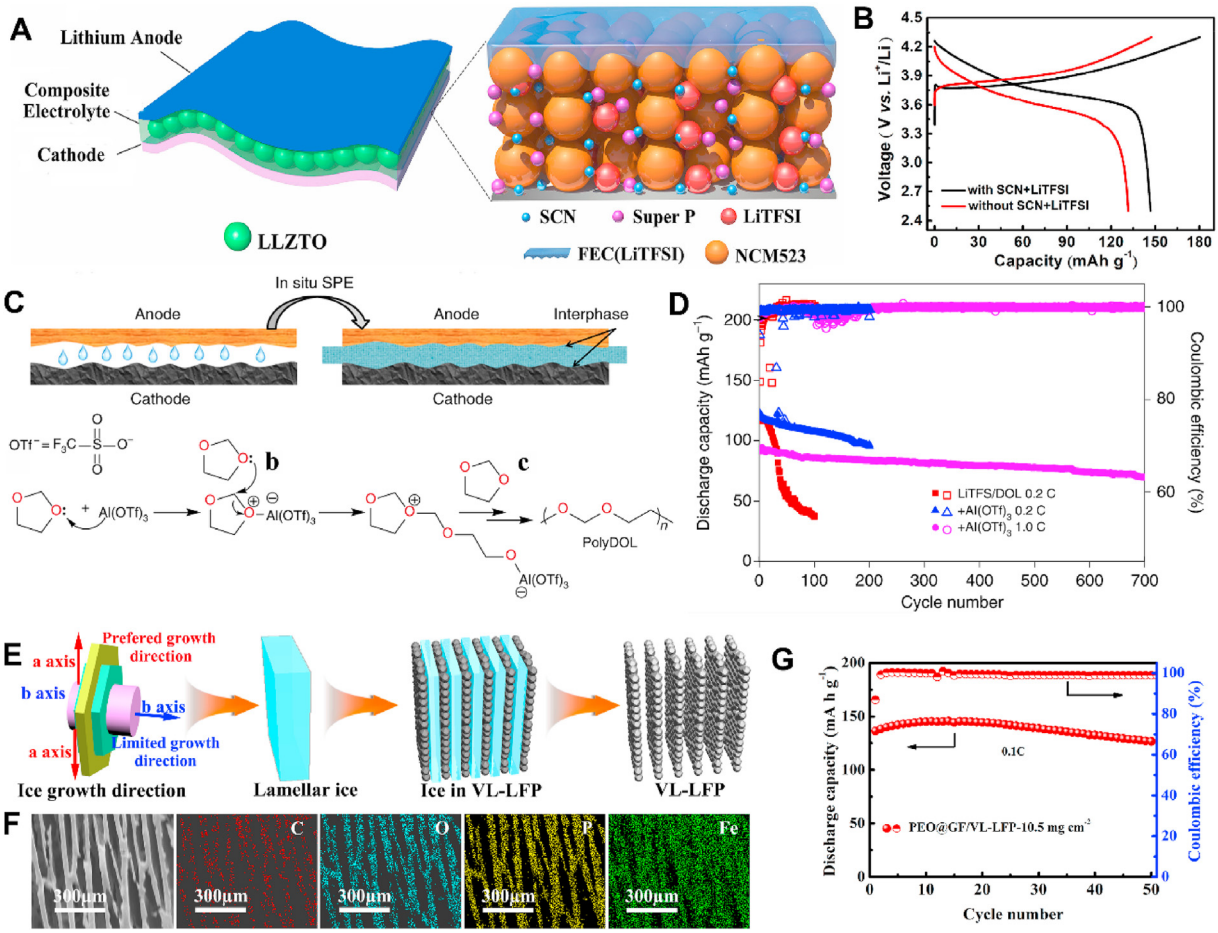

Fig. 2. (A) Schematic of a Li-NCM523 ASSLB with SCN + LITFSI in the cathode. (B) Comparison of the charge-discharge curves of the cells with and without SCN + LITFSI in the cathode. Reproduced with permission [31], Copyright 2019, Elsevier Ltd. (C) Schematic of in-situ polymerizing polyDOL and relevant polymerization mechanism. (D) Cycling performance of Li/polyDOL/LFP and Li/DOL//LFP cells. Reproduced with permission [33], Copyright 2019, Nature Publishing Group. (E) Fabrication illustration and mechanism of VL-LFP electrode (F) SEM images of VL-LFP electrode and corresponding elemental mappings. (G) Cycling performance of Li/PEO@GF/VL-LFP ASSLB with an LFP loading of 10.5 mg cm^{-2}. Reproduced with permission [34], Copyright 2019, Elsevier Ltd.

During this process, the precursor solution fills the gap between anode and cathode, pores in the cathode and separator and sufficiently wets the electrodes (as illustrated in Fig. 2C). When the polymerization process occurs, an SPE network is formed between anode and cathode (working as the separator) and in the cathode (working as the Li^+ transport pathway) concurrently, thus reducing the interfacial resistance and facilitating Li^+ transport in the cathode as well. For instance, Archer's group reported ring-opening polymerization of 1,3-dioxolane (DOL) with the assistance of an $Al(OTf)_3$ initiator. The in-situ polymerization occurred inside an electrochemical cell to produce a polyDOL SPE, which retains conformal interfacial contact with all cell components as well as facilitates Li^+ transport in the cathode (Fig. 2D). The assembled 5 mg cm^{-2} LFP loaded Li-LFP ASSLBs demonstrated high Coulombic efficiency (CE, 99%) and long cycling life (>700 cycles) at 1C with the in-situ polymerization design [33].

As we mentioned above, the high tortuosity of the Li^+ transport pathway is another critical factor that limited the electrochemical performance of thick electrodes. In this regard, our group developed a vertically-aligned LFP electrode (labeled as VL-LFP) with reduced tortuosity using a freeze-drying method. The fabrication mechanism was illustrated in Fig. 2E. Based on the understanding of ice anisotropic growth kinetics, the growth rate along the a-axis is over 10^3 times that along the b-axis, resulting in lamellar ice morphology. During the freeze-drying process, the lamellar ice acted as the in-situ template and pressed electrode materials into the lamellar structure. After the ice removal, a VL-LFP cathode with a vertically-aligned structure is obtained (see SEM images and mappings in Fig. 2F). Benefitting from the reduced tortuosity for facilitating Li^+ transport in the cathode, the ASSLBs assembled with VL-LFP cathode demonstrated improved rate performance (100 mAh g^{-1} at 1C) compared with the LFP cathode from directly drying method (50 mAh g^{-1} at 1C), where LFP loading was 6 mg cm^{-2}. Moreover, as shown in Fig. 2G, the ASSLBs assembled with 10.5 mg cm^{-2} VL-LFP cathode delivered a high capacity of 145 mAh g^{-1} and stably run for 50 cycles at 0.1C, equaling to an areal capacity of 1.52 mAh cm^{-2} [34].

In brief summary, the introduction of SPEs during electrode fabrication ensures fast Li^+ transport through thick electrodes. Moreover, building continuous Li^+ transport pathways with reduced tortuosity (eg. vertically aligned channels) is expected to further enhance the capacity output as well as rate performance. It is worth mentioning that the introduced SPEs fill the cathode pores, reducing the energy density, which should be balanced in the practical application. Further improving the ionic conductivity of the SPEs would be a great direction to reduce the SPE content based on ensuring good Li^+ transport in the thick electrodes.

2.2. Oxide electrolyte systems

2.2.1. Building fast Li-ion transport channels

Compared with SPEs (10^{-8}–10^{-6} S cm^{-1} at RT), oxide SSEs possess higher ionic conductivity (10^{-3} S cm^{-1} at RT), which endow them with a greater possibility to pursue low-temperature ASSLBs. One particular issue is that the rigid oxide particles can hardly build an interconnected Li^+ conductive network at RT. The large contact resistance among the oxide particles restricts them from being directly introduced to the electrode as the ionic conductors. In most cases, an annealing process (typically over 1000 °C) is required to weld the oxide particles to reduce the contact resistance [35,54]. Under this situation, most of the electrode materials and conductive additives are unable to tolerate the high temperatures. Thus, the electrode materials and conductive additives are post-introduced into the porous scaffold of oxide SSEs instead of mixing them together before annealing. In this regard, the fabrication of porous oxide SSE scaffolds is critical to fabricating thick oxide SSE-based electrodes.

Among various oxide SSEs, garnet-type SSEs (eg. LLZO, $Li_7La_{2.75}Ca_{0.25}Zr_{1.75}Nb_{0.25}O_{12}$ (LLCZNO)) show higher stability against Li and polysulfides compared with NASICON-type (eg. $Li_{1+x}Al_xTi_{2-x}(PO_4)_3$ (LATP), $Li_{1+x}Al_xGe_{2-x}(PO_4)_3$ (LAGP)) and perovskite-type (eg. $Li_{0.34}La_{0.56}TiO_3$ (LLTO)) SSEs. Hence, many researchers have dedicated their efforts to garnet SSEs in ASSLBs, including solid-state Li–S batteries (SSLSBs) [55]. For instance, Hu's group developed a bi-layered LLCZNO SSE via tape-casting method, where a porous layer was sintered on the dense supporting SSE layer (Fig. 3A). According to the scanning electron microscopy (SEM) images, the thickness of the porous layer is 70 μm, which was fabricated by annealing the pallet consisting of LLCZNO and poly(methyl methacrylate) (PMMA) pore-forming agent. The porous layer can act as the interconnected Li^+ conductive network for active material (sulfur) and carbon additive infusion. The dense SSE layer was determined to be 35 μm, which acted as a physical barrier to suppress polysulfides shuttle (a small amount of liquid electrolyte was added to reduce the interface resistance between the electrolyte and electrode). Due to the interconnected Li^+ conductive network, with a high sulfur loading of 7.5 mg cm^{-2}, the assembled SSLSBs deliver a capacity of around 600 mAh g^{-1} as well as a high average CE of 99% at 0.2 mA cm^{-2} [35]. In another case, Wachsman's group reported a similar bi-layered LLZO structure, where a porous LLZO textile was realized by a templating method. In their work, a cellulose textile was chosen as the template for LLZO precursor impregnate. After calcination of the precursor impregnated template in oxygen, the template was removed and an LLZO textile was achieved (Fig. 3B). Similar to Hu's work, the porous LLZO textile was sintered on a dense LLZO pallet, where the LLZO textile acted as the host for sulfur and carbon additives (Fig. 3C). Due to fast Li^+ transport along the LLZO fibers, the assembled SSLSBs exhibited improved electrochemical performance. The SSLSB assembled with 10.8 mg cm^{-2} loaded cathode delivered a reversible capacity over 1000 mAh g^{-1} after 40 cycles at 0.1C (Fig. 3D). Upon further increasing the sulfur loading to 18.6 mg cm^{-2}, a high capacity of over 800 mAh g^{-1} is retained. The high capacity output coupled with a thin SSE of 20 μm endows the

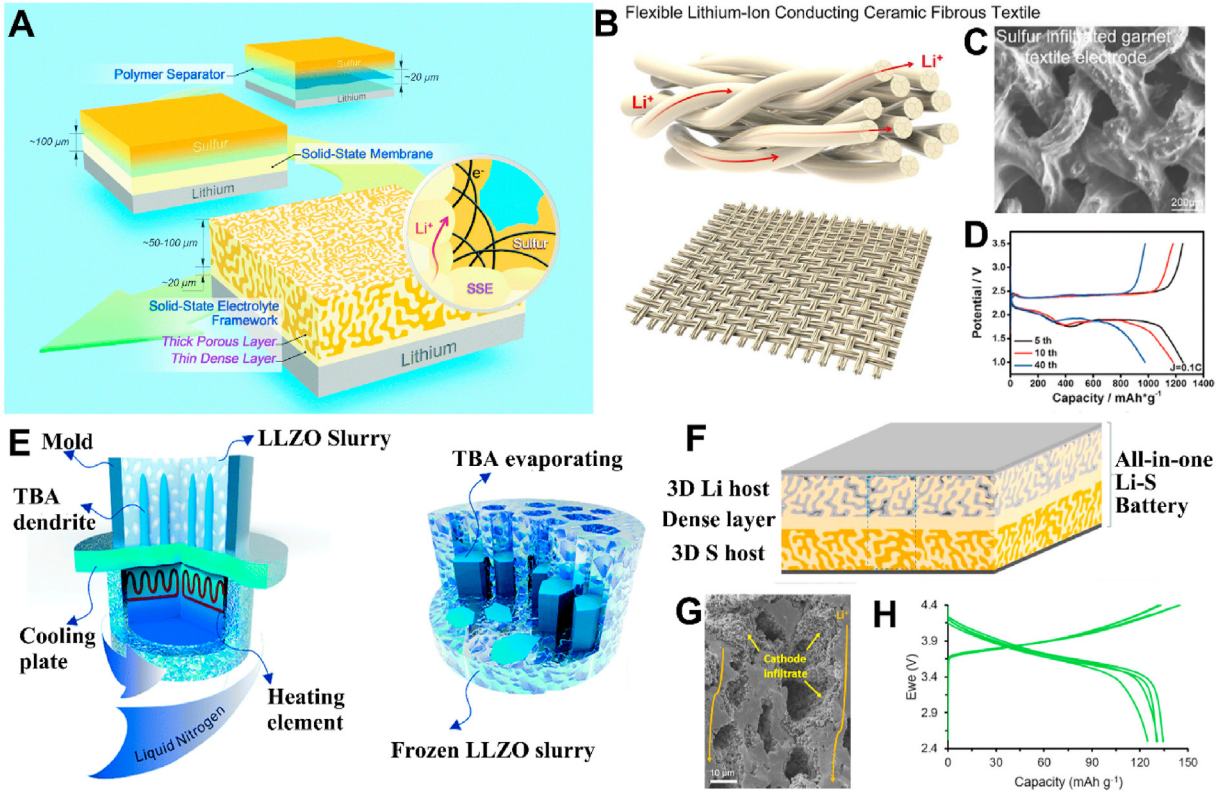

Fig. 3. (A) Schematic illustration of a bilayer SSE framework in comparison with traditional polymer separators and rigid SSE architectures. Reproduced with permission [35], Copyright 2017, Royal Society of Chemistry. (B) Schematic illustration of a flexible garnet textile. (C) SEM image of the sulfur cathode infiltrated garnet textile. (D) Charge-discharge profiles of the assembled SSLSBs with a sulfur loading of 10.8 mg cm^{-2} at 0.1C. Reproduced with permission [36], Copyright 2018, Elsevier Ltd. (E) Freeze casting apparatus and formation of the porous LLZO by freeze-drying. Reproduced with permission [38], Copyright (2019) Royal Society of Chemistry. (F) Schematic illustration and (F) cycling performance of the all-in-one SSLSBs. Reproduced with permission [39], Copyright 2018, Elsevier Ltd. (G) Vertically-aligned structured cathode with fast Li^+ transport pathways. (H) Charge-discharge profiles of the assembled Li-NMC622 SSLBs. Reproduced with permission [41], Copyright 2020, American Chemical Society.

SSLSBs with a high energy density of 352 Wh kg^{-1} [36]. In another study, Xu and his coworkers reported a similar bi-layered LATP framework for NMC 811 infusion. The thickness of the cathode was determined to be ~200 μm (NMC811 loading: 13.1 mg cm^{-2}). To reduce the interfacial resistance between the active material and SSE in the cathode as well as inhabit the side reaction between LATP and Li anode, an SPE (polyethylene glycol bis(amine)-triglycidyl isocyanurate (NPEG-TGIC)) was introduced into the system. In the porous layer, it works as the Li^+ bridge to facilitate the Li^+ transport between LATP and cathode materials. Moreover, it also serves as a buffer layer to suppress the side reactions between the Li metal anode and LATP. Benefitting from the rationally designed structure, the Li/NMC811 with a 13.1 mg cm^{-2} NMC811 delivered a high capacity of 153 mAh g^{-1} (operating voltage window: 2.5–4.3 V, testing rate: 0.1C), equaling to an areal capacity of 2.01 mAh cm^{-2}. It also should be mentioned that the cell presented high capacity retention of 70% after 50 cycles and the electrolyte used in this cell is only 80 μm, presenting a promising application perspective. More importantly, attributing to the high oxidization stability of NPEG-TGIC, the cell presented high stability over 4.7 V and delivered a higher capacity of over 210 mAh g^{-1} at 0.1C, which will pave the way for perusing high-energy-density and high-voltage SSLBs [37].

As we mentioned above, the Li^+ transport capability in thick electrodes is also related to the tortuosity of Li^+ transport channels. With this in mind, Doeff and his coworkers fabricated vertically-aligned channels in the porous LLZO pallet to reduce the Li^+ transport distance via a freeze casting technique. In their protocol, *tert*-butyl alcohol (TBA) was chosen as the solvent. It was frozen in-place and worked as the in-situ template during freezing (Fig. 3E). After TBA solvent removal, the vertically-aligned channels were formed in the porous LLZO pallet, which functioned as an interconnected Li^+ conductive host for active materials infusion. Coupling the porous LLZO host infused with NMC622 cathode and a dense LLZO film (20 μm) obtained by tape casting, the assembled Li-NMC622 SSLBs demonstrated good electrochemical performance. Under a high cutoff voltage of 4.7 V, the SSLBs assembled with a 15.7 mg cm^{-2} NMC622 loaded cathode demonstrated a high initial capacity of 175 mAh g^{-1} and high capacity retention of 72% after 90 cycles at 0.3 mA cm^{-2} [38].

To further reduce the interfacial resistance at the anode side, another porous layer was introduced to build an all-in-one structure. As shown in Fig. 3F, the bottom and upper porous SSE layers were used for Li and cathode materials accommodation, while the middle dense layer functioned as the SSE to transport Li^+ as well as separate the cathode and anode [39,40]. Benefitting from the 3D structure in both anode and cathode sides, the unique structure possesses several advantages in terms of Li^+/e^- transport, low localized current densities and volume change confinement. Equally important, based on the all-in-one structure, the cell manufacturing process becomes facile by simply sealing the anode-SSE-cathode integration structure into a package. As proof of the concept, with a sulfur loading of 5.4 mg cm^{-2}, the assembled SSLSBs delivered a high discharge capacity of 1200 mAh g^{-1} at 50 mA g^{-1} and stably run for 50 cycles [39]. To further reduce the tortuosity of Li^+ transport and shorten the Li^+ diffusion distance, a freeze-tape-casting technique was developed by Doeff's group. Similar to the mechanism of freeze-drying we mentioned in section 2.1, a vertically-aligned porous LLZO structure was achieved and subsequently resulted in facilitating Li^+ transport (Fig. 3G). As a result, with a high cathode thickness of 120–130 μm, the assembled Li-NMC622 ASSLBs delivered a high capacity of 125–135 mAh g^{-1} at 0.1C (operating at RT, Fig. 3H). It is noteworthy that the active material loading is only 4–5 mg cm^{-2} due to the low pore occupancy. Considering the potential of the pores to accommodate 35–40 mg cm^{-2} NMC622 (80–90% pore occupancy), there is still plenty of room to further improve the electrochemical performance [41].

2.2.2. Creating favorable SSE/cathode material interface

In section 2.2.1, we have summarized recent progress on designing fast Li^+ transport channels in thick electrodes to improve electrochemical performance. In this section, we will discuss the effect of the interface on thick electrode design and the relationship between structure and electrochemical performance. It is well known that the mismatched solid-solid interface between rigid oxide SSEs and active materials is one of the biggest issues that hinder the development of all-oxide-SSE-based ASSLBs. In the thick electrode, a well-matched interface is also a prerequisite for guaranteeing good electrochemical performance. Nevertheless, the formation of a passivated Li_2CO_3 layer on the surface of garnet SSEs because of air exposure, where Li_2CO_3 possesses poor ionic conductivity, results in large interfacial resistance [56]. To solve this problem, Wang and his coworkers reported a novel low melting-point $Li_{2.3}C_{0.7}B_{0.3}O_3$ additive to in-situ form an intermediate phase (Fig. 4A). Here, the $Li_{2.3}C_{0.7}B_{0.3}O_3$ additive played two important roles: 1) it can react with Li_2CO_3 to form a $Li_{2.3-x}C_{0.7+x}B_{0.3-x}O_3$ interface, which presents a higher ionic conductivity than that of Li_2CO_3 by several orders of magnitude, promoting Li^+ transport at the interface; 2) the $Li_{2.3}C_{0.7}B_{0.3}O_3$ additive possesses a low melting point of 690 °C, the thermal soldered LCO and LLZO by melted LCBO show better wettability at the cathode interface. As a result, the all-ceramic LCO/LLZO/Li cell with the help of interface engineering delivered a stable capacity of 83 mAh g^{-1} over 100 cycles under 0.05C at 25 °C (Fig. 4B) [57]. In another study, Zhang and his co-workers reported a lithium donor reaction to decarbonate LLZTO and convert the Li_2CO_3 layer into an active LCO coating layer on the LLZTO surface. The LCO coating showed high stability against air and further prevented the formation of Li_2CO_3. Based on this strategy, the LCO-LLZTO@LCO composite cathode demonstrated 81% capacity retention after 180 cycles at 0.1C [58]. Conversion of the non-conductive Li_2CO_3 layer into higher conductive layers or active materials is an effective strategy to solve the interface issue and is expected to improve the electrochemical performance of garnet-based ASSLBs.

In another case, a rapid, high-temperature microwave soldering process was proposed by Hu's group to reduce the electrode (V_2O_5+carbon black)/SSE interfacial resistance. As illustrated in Fig. 4C, before the microwave soldering process, there are many voids in the cathode materials and a big gap between cathode and garnet SSE, resulting in poor contact and big interfacial resistance. After a microwave treatment at 1200 K for only 3s, the melted V_2O_5 filled into the voids and gap and formed a dense cathode and soldered V_2O_5/garnet interface. Benefitting from the good V_2O_5/SSE, V_2O_5/carbon black interfaces and the continuous cathode layer, the interfacial resistance was 28 times reduced compared with the untreated one (0.5 kΩ cm^{-2} vs 14.4 kΩ cm^{-2}). As a consequence, the assembled Li/SSE/V_2O_5 delivered a high discharge capacity of 80 mAh g^{-1} when cycled at 116 mA g^{-1} for 20 cycles and 48 mAh g^{-1} when cycled at 290 mA g^{-1} for 10 cycles [59]. One key issue is that the cathode is an SSE-free structure, which limits the Li^+ transport in the cathode, thus the ASSLBs should be operated at a high temperature of 100 °C. The electrochemical performance and active material loading have the potential to be further improved via cathode structure optimization.

Recently, Nan's work discovered epitaxial interfaces formed between perovskite solid electrolytes and Li-rich layered electrodes when sintering the amorphous LLTO and $0.54Li_2TiO_3$-$0.46LiTiO_2$ (labeled as LTO) electrode powders at 1250 °C for 6 h. After sintering, the amorphous LLTO crystallized on the surfaces of LTO

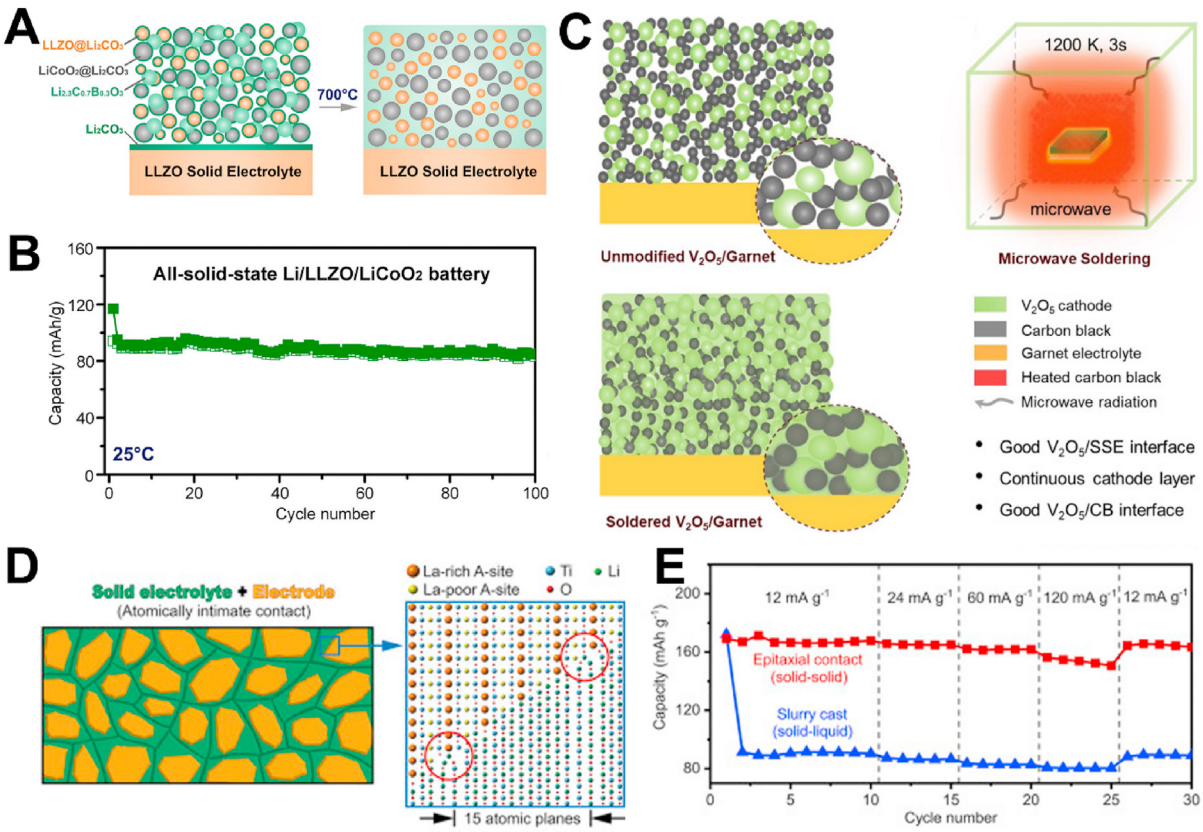

Fig. 4. (A) Schematic illustration of interfacial engineering to covert Li_2CO_3 into $Li_{2.3-x}C_{0.7+x}B_{0.3-x}O_3$ interface and (B) the cycling stability of the assembled ASSLBs at 0.05C. Reproduced with permission [57], Copyright 2018, Cell Press. (C) Comparison of the structure and interface of the electrode before and after rapid microwave soldering. Reproduced with permission [59], Copyright 2020, Elsevier Ltd. (D) Schematic illustration of the atomically intimate solid-solid electrode-electrolyte contact. (E) Comparison of rate performance of the ASSLB based on epitaxial contact electrode with a liquid cell using slurry casting electrode. Reproduced with permission [42], Copyright 2019, Cell Press.

particles. It was observed that electrode materials were embedded within the lattice of SSE after treatment, attributing to an intimate interface contact (Fig. 4D). The intimate contact solid-solid composite electrode displayed high-rate performance, even surpassing its counterpart based on solid-liquid contact. As shown in Fig. 4E, with a high loading LTO of 9.3 mg cm^{-2}, the ASSLB based on epitaxial solid-solid contact delivered a high initial capacity of ~170 mAh g^{-1} at 12 mA g^{-1} and maintained 92.2% of its initial capacity (156 mAh g^{-1}) when the current density raised to 120 mA g^{-1}. For comparison, the cell based on solid-liquid contact only delivered a lower capacity of roughly 80 mAh g^{-1} (operating temperature: 60 °C) [42]. This discovery pointed out a new strategy for addressing the solid-solid electrode-electrolyte contact issue and has the potential to be shifted to other perovskite solid electrolytes and layered electrode materials. In another study, Hu's group developed ultrafast high-temperature sintering (UHS) process to fabricate ceramic materials by radiative heating under an inert atmosphere [54,60]. The UHS process can be completed in 10s and transform the ceramic powders into a dense pellet. The UHS process has demonstrated its universality in fabricating various ceramic SSEs (eg. LLZO, $Li_7Nd_3Zr_2O_{12}$, $Li_7La_3Sn_2O_{12}$, $Li_7Pr_3Zr_2O_{12}$). Moreover, the obtained ceramic pellets presented high ionic conductivities and excellent Li dendrite suppression capabilities. Even though it hasn't been applied to fabricate cathodes, which has a big potential to be used to fabricate SSE-containing cathodes with reduced interfacial resistance [54].

To sum up, in oxide-SSE-based ASSLBs, there are two main strategies to improve the electrochemical performance of thick electrodes: (1) the construction of fast Li^+ transport channels and (2) interfacial engineering. For the former, a widely adopted electrode fabrication process is infusing the electrode materials into a porous SSE scaffold. To reduce the contact interfacial resistance, in most cases, SPEs or liquid electrolytes should be introduced. The introduction of liquid electrolytes will lower the safety, while the low ionic conductivity SPE forces the ASSLBs to be operated at high temperatures. Another consideration that should be taken is that it is challenging to fill all the pores of the scaffolds, resulting in limited active material contents and subsequently lower energy densities. In terms of interfacial engineering, it has demonstrated its potential for all-ceramic ASSLBs fabrication. Nevertheless, the electrochemical performance is still limited due to the low ionic conductivity of the interface layer. The electrochemical performance has the potential to be further improved by exploring new strategies to create intimate contact between the SSE, active materials, and conductive materials. Generally speaking, all-oxide SSE-based ASSLBs are still in their infancy and more efforts should be devoted to improving their electrochemical performance.

2.3. Sulfide and halide electrolyte systems

2.3.1. Creating favorable SSE/cathode material interface

The sulfide- and halide-electrolyte-based ASSLB system is quite different from the aforementioned two systems. In most cases, the sulfide- and halide-electrolyte-based ASSLBs are tested in a model cell. During the assembly process, several tons of pressure will be added to press the electrolyte or cathode materials powders into a pallet to build continuous Li^+ transport pathways [61,62]. Even in pouch cells, high pressure is still required [23]. The aforementioned

3D structures for facilitating Li^+ transport will be destroyed by the applied pressure. With this in mind, the construction of 3D structures for the thick sulfide-electrolyte-based cathode is rarely reported. Instead, creating an intimate SSE/cathode material contact interface is a more promising direction, which is widely used to improve ion transport and charge transfer in thick electrodes. In the liquid battery systems, even though no electrolyte was introduced into the cathode during cathode fabrication, the cells can still work well due to the continuous Li^+ transport pathways built by the flowable liquid electrolyte. Inspired by this, SSE solutions obtained by dissolving the SSEs into suitable solvents were reported to fabricate fast Li^+ pathways in thick cathodes [43,63]. For instance, Wang's group reported a composite Li_2S cathode with a well-built tri-phase interface of Li_2S, SSE and carbon conductive based on a solution-processable Li_6PS_5Cl SSE (Fig. 5A). The results showed that the Li_6PS_5Cl SSE and Li_2S were uniformly embedded by a carbon matrix in nanoscale, enabling a mixed ionic/electronic conductive Li_2S electrode for SSLSBs. With a high Li_2S loading of 3.6 mg cm^{-2}, as shown in Fig. 5B, the assembled SSLSBs exhibited a reversible capacity of 830 mAh g^{-1} within 60 cycles at 50 mA g^{-1} [43]. Besides the Li_6PS_5Cl SSE, $Li_7P_3S_{11}$ was also reported as another solution accessible SSE and demonstrated its capability to reduce the interfacial resistance in SSLBs [19,64]. Xu's group reported to in-situ grew a thin $Li_7P_3S_{11}$ SSE layer on the surface of Co_9S_8 active material, where the anchored $Li_7P_3S_{11}$ SSE presented an ultra-small particle size of around 10 nm, resulting in an increased contact area and intimate contact interface between the electrolyte and active materials. As a result, the assembled SSLSBs showed excellent cycling stability within 1000 cycles [19].

To smoothly transfer the conventional electrode fabrication technique into SSLBs and solve the interfacial issues, a facile SSE infusion method was developed to build interconnected Li^+ transport pathways in SSLBs [44,45,65]. Park's group chose ethanol as the solvent to firstly dissolve their Li_6PS_5Cl SSE and developed liquified Li_6PS_5Cl SSE solution with high flowability. Subsequently, it was infused into an NMC622 cathode (obtained by conventional slurry casting method and no electrolyte in it, Fig. 5C). After removing the solvent at 180 °C, a continuous SSE phase was formed to fill the pores of the NMC622 cathode and act as Li^+ transport pathways. Benefitting from the well-built Li^+ transport pathways, the assembled SSLBs with a high NMC622 loading of 17 mg cm^{-2} delivered a high capacity of 136 mAh g^{-1} [44]. Nevertheless, it should be noted that the operating current density is only 0.05C and the operating temperature is 90 °C, which restricts its practical application to some extent. To understand the limitation, Jung and his coworkers investigated the ionic conductivity-annealing temperature relationship in argyrodite type electrolytes. It is found that the ionic conductivity of $Li_6PS_5Cl_{0.5}Br_{0.5}$ SSE is recoverable and highly dependent on the post-treatment temperature. Ionic conductivities of 0.4 mS cm^{-1} and 2.0 mS cm^{-1} were achieved by heat-treated at 180 °C and 400 °C, respectively. Unfortunately, some of the components such as binders in the electrolyte and electrodes can hardly tolerate such a high temperature of 400 °C, thus a relatively low temperature of 180 °C is more reasonable in practical application. With the help of reducing the SSE thickness and subsequently reducing the internal resistance, the assembled cells still have the potential to be operated at RT. For instance, in this work, the assembled graphite/NMC622 SSLB with a thin SSE (40 μm) delivered a high capacity of 146 mAh g^{-1} at 0.1C (Fig. 5E), equaling to an areal capacity of 1.2 mAh cm^{-2} with a heat-treated temperature of 180 °C (operating temperature: 30 °C). More importantly, the liquified SSE infusion method also shows great potential to match it with the state-of-the-art Li-ion battery manufacturing line. The anode, separator, the cathode can be packed into a traditional pouch cell and then injecting the liquified SSE into the package to wet all components and build Li^+ transport pathways, a pouch cell is obtained after solvent removal (Fig. 5D). One issue for this project is that the $Li_6PS_5Cl_{0.5}Br_{0.5}$ SSE requires a high temperature to recover its high ionic conductivity, which put forward high requirements in choosing suitable binders, separators and sealing packages, etc. In practical application, it will inevitable to sacrifice some ionic conductivity, which will affect the electrochemical performance such as rate-performance and capacity output for thick cathode-based SSLBs [45]. Compared with argyrodite-type SSEs, the temperature for Li_3InCl_6 for recovering its ionic conductivity is much lower. According to our report, only a temperature of

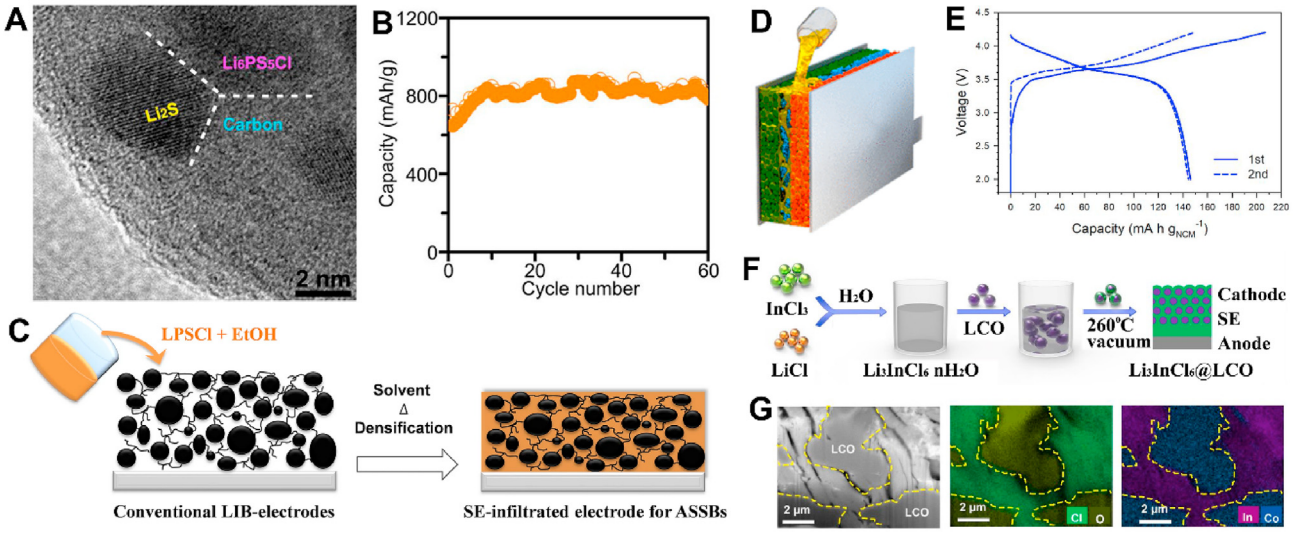

Fig. 5. (A) The high-resolution TEM image of Li_2S–Li_6PS_5Cl–C nanocomposite and (B) the cycling performance of the assembled SSLBs at 50 mA g^{-1}. Reproduced with permission [43], Copyright 2016, American Chemical Society. (C) Schematic illustrating fabrication of cathode within SSE solution infusion method. Reproduced with permission [44], Copyright 2019, Nature Publishing Group. (D) Schematic illustrating fabrication of SSLBs by injection of liquefied $Li_6PS_5Cl_{0.5}Br_{0.5}$ SSE. (E) Charge-discharge profiles of NCM622/graphite SSLB with a heat-treated temperature of 180 °C. Reproduced with permission [45], Copyright 2020, American Chemical Society. (F) Schematic illustration of the in-situ synthesis of Li_3InCl_6 on LCO. (G) Cross-sectional SEM image of LIC@LCO-15 wt% coupled with Elemental mappings of O and Cl. Reproduced with permission [46], Copyright 2020, Elsevier Ltd.

130 °C is enabled to recover the ionic conductivity to 1.17 mS cm^{-1} at 25 °C, which is 57% of its intrinsic ionic conductivity obtained at 200 °C (2.04 mS cm^{-1}) [16]. The lower temperature means more choice and less harsh conditions in choosing binders, sealing packages, etc. The potential application in liquified SSE infusion strategy was proved by our previous work, where Li_3InCl_6 was dissolved into water as a coating solution for LCO cathode fabrication (Fig. 5F). The results showed that only a low Li_3InCl_6 content of 15 wt% is enough to well-cover the LCO particles (Fig. 5G). Dependent on the reduced interfacial resistance and high ionic conductive coating material, the assembled Li-LCO SSLB with a high LCO loading of 48.7 mg cm^{-2} delivered a high areal capacity of 6 mAh cm^{-2} at 0.13 mA cm^{-2} [46]. Despite the merits of liquified SSE in fabricating continuous and uniform Li^+ transport pathways, it is only suitable for the recoverable SSEs (eg. $Li_7P_3S_{11}$, Li_6P_5Cl, Li_3InCl_6) after solvent removal [19,43,45,46]. For other SSEs such as Li_3YCl_6, the recovery products are LiCl and YCl_3 after water removal. The poor ionic conductivity of the recovery products restricts the application of Li_3YCl_6 as a candidate for the liquified SSE infusion method [66]. Besides the concern on the post-treated temperature, the compatibility of SSE and liquified SSE with the electrode materials, current collectors and sealing packages should be also carefully considered. For instance, a Li_3InCl_6 aqueous solution is strongly acidic, which will result in corrosion of the Al current collector and Al plastic film pouch cell bag [67]. Additionally, according to Mo's simulation result, Li_3InCl_6 possesses a high reduction potential of around 2.38 V, which pales in comparison to Li or graphite anodes [68].

2.3.2. Enhancement of cathode material electrochemical kinetics

The properties of cathode materials such as particle size or crystal structure also have a great effect on Li^+ transport and subsequent electrochemical performance. For instance, Ceder and his coworkers investigated the effect of both cathode material size and electrolyte size on the Li^+ transport pathways building in the cathode. As shown in Fig. 6A, using 5 μm NMC532 (labeled as $D_{CAM} = 5$ μm) as the research objective, it is found that the smaller size $75Li_2S{-}25P_2S_5$ (LPS) of 3 μm (labeled as $D_{SE} = 3$ μm) helps construct a more uniform Li^+ transport scaffold compared with its counterpart with a size of 5 μm. As a result, the ASSLB with a 3 μm LPS built cathode delivered a higher capacity of ~150 mAh g^{-1} at 0.05 mA cm^{-2}, which is 25 mAh g^{-1} higher than its counterpart. Further increasing the size of SSE to 8 μm, the capacity was further decreased to 75 mAh g^{-1}, where the NMC532 content was controlled as 60 wt%. Interestingly, the size effect of the cathode material is opposite in comparison with SSE size. Due to the lower exposed surface of larger cathode material, less SSE is needed to cover its surface to transport Li^+. With the same content of SSE in the cathode, the SSE with large cathode material can build more favorable Li^+ transport pathways. For instance, using 3 μm LPS as the electrolyte, the ASSLB with 5 μm NMC532 delivered a capacity of 75 mAh g^{-1}, which is 50 mAh g^{-1} lower than 12 μm NMC532. With this in mind, in practical application, to realize high capacity output, smaller size SSE and larger size cathode material are preferred. According to Ceder's results, as illustrated in Fig. 6A, to achieve a high cathode material utilization of more than 90%, a λ ($\lambda = D_{CAM}/D_{SE}$) higher than 1.5 is recommended, where the cathode material content can reach as high as 70 wt% [69].

Besides the effect of cathode material and SSE size on building Li^+ transport pathways, the crystal structure of cathode materials also shows its influence on the electrochemical performance of thick electrodes [70–72]. Our group investigated the Li^+ transport capability difference of single-crystal NMC532 (labeled as SC-NMC532) and polycrystal NMC532 (labeled as PC-NMC532) in ASSLBs. As illustrated in Fig. 6B, many grain boundaries can be observed in the PC-NMC532. Li^+ should pass through many grain boundaries before reaching the SSE, limiting the Li^+ transport rate in the cathode material. On the contrary, the continuous Li^+ transport pathways in the SC-NMC532 guaranteed fast Li^+ transport through the cathode materials, enabling faster Li^+ kinetics. As proof of the concept, the SC-NMC532 delivered 6–14 times higher Li^+ diffusion coefficient than that of PC-NMC532. Owing to the faster Li^+ transport capability, the ASSLBs using SC-NMC532 cathode showed better electrochemical performance compared with their polycrystalline counterpart. The ASSLBs assembled with SC-NMC532 delivered an initial specific capacity of 156.4 mAh g^{-1} at 0.13 mA cm^{-2} and maintained 52.4% of its initial capacity (82 mAh g^{-1}) when the current density raised to 1.3 mA cm^{-2}, while the relative capacities of PC-NMC532 at 0.13 mA cm^{-2} and 1.3 mA cm^{-2} are only 127.5 mAh g^{-1} and 2.1 mAh g^{-1}, respectively (Fig. 6C) [72]. With this in mind, before optimizing the cathode structure and interface, it is necessary to optimize the electrode materials and electrolytes first.

2.3.3. Alleviating the deterioration effect of binder and solvent

In practical application, slurry casting is one of the widely adopted methods for large-size sheet type electrode fabrication, the effect of binder and solvent should be carefully considered. As shown in Fig. 7A~B, Zhang and his coworkers fabricated an NMC811-Li_6PSCl_5 electrode based on the slurry casting method using ethyl cellulose as the binder and systematically investigated the binder effect. They found that the introduction of binder attributed to a tight contact between SSE and active materials, thus facilitating Li^+ transport through the SSE/active material interface. As a result, the discharge capacities have been improved to varying degrees with binder content ranging from 0.5 wt% to 1 wt% compared with the binder-free electrode. Further increasing the binder content to over 2 wt%, the excess binder in the electrode hindered the ion transport and charge transfer, which reduced utilization of NMC811 active materials and deteriorated the discharge capacity [73]. With this in mind, in practical application, the binder is essential by taking the mechanical properties and electrode material/SSE contact into consideration. Nevertheless, the binder content should be controlled in a reasonable range because the non-ionic and non-electronic conductive excess binder will block the Li^+/e^- transport and result in deteriorated electrochemical performance. To solve the binder effect issue, a post-heat treatment was applied to remove the binder in the electrode. As shown in Fig. 7C, a similar slurry casting process (with binder) was adopted to gain the electrodes, where the binder enabled the electrode materials with imitating contact and mechanical properties during electrode fabrication. Afterward, the binder was removed with a heating temperature of 225 °C for 30 min under vacuum. Compared with the binder-containing electrode, the binder-free electrode showed a better rate performance. Even at a high current density of 3 mA cm^{-2}, the SSLBs assembled with a binder-free NMC111 electrode using In as the anode still delivered a high capacity of 50 mAh g^{-1}, which is much higher than its counterpart containing binder (15 mAh g^{-1}). More importantly, to demonstrate its potential in practical application, a high energy density of 115 Wh kg^{-1} was achieved at the cell level, where NMC 111, SSE, graphite thicknesses were controlled as 74, 59, and 134 μm, respectively, equaling to high active materials loadings of 16.3 and 12.4 mg cm^{-2} in the cathode and anode [47].

Besides the binder effect, the solvent effect is also of significance towards sulfide- and halide-based SSLBs. As we mentioned in section 2.3.1, the dissolution of SSE is beneficial for creating an intimate SSE/active material interface and reducing the interfacial resistance. However, one issue is that a high annealing temperature is needed to recover a high ionic conductivity. Some of the

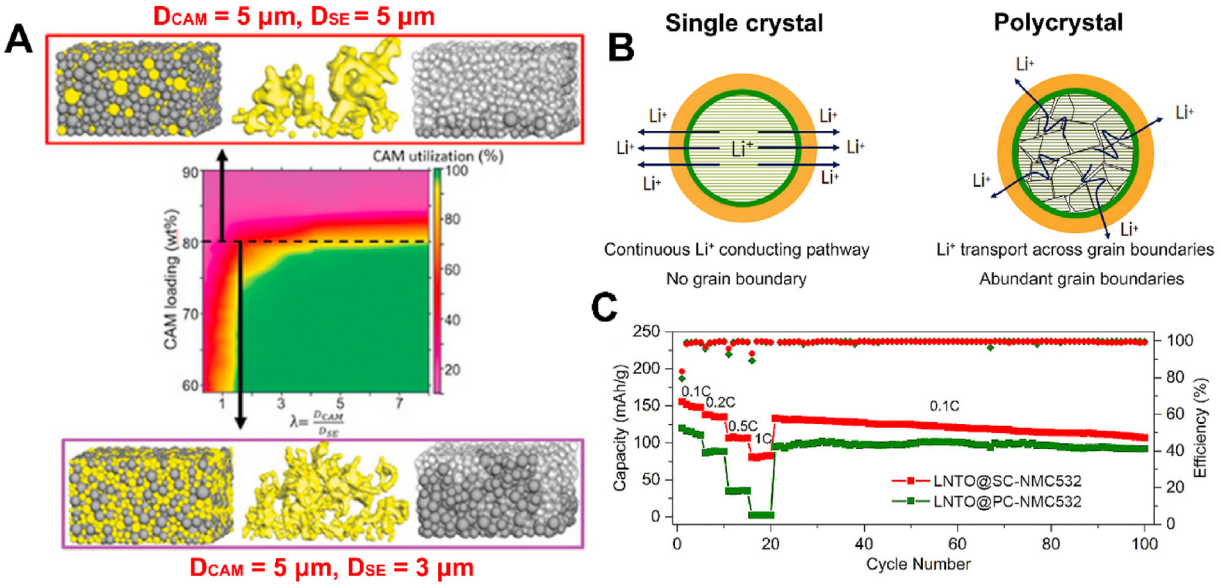

Fig. 6. (A) The size effect of cathode active material (CAM) and SSE in building Li^+ transport scaffold and CAM utilization. Reproduced with permission [69], Copyright 2020, Wiley-VCH. (B) Comparison of Li^+ transport in single-crystal and polycrystal. (C) Rate performance of SSLBs assembled with single-crystal NMC532 and polycrystal NMC532. Reproduced with permission [72], Copyright 2020, Elsevier Ltd.

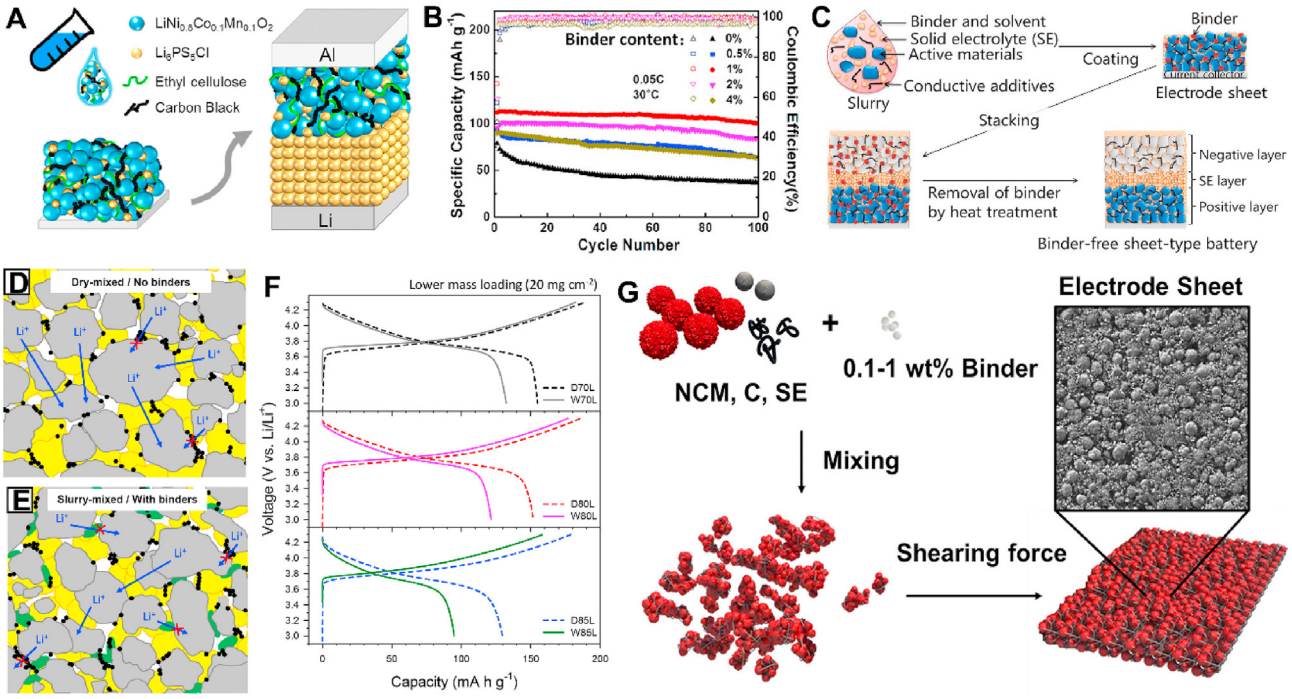

Fig. 7. (A) Schematic illustration of an SSLB assembly with a slurry casting electrode and (B) the electrochemical performance comparison with different binder content in the electrode. Reproduced with permission [73], Copyright 2020, Elsevier Ltd. (C) Schematic illustration of the fabrication process for binder-free sheet-type SSLBs. Reproduced with permission [47], Copyright 2018, Nature Publishing Group. Schematic illustration of Li^+ transport in the (D) dry-mixing electrode and (E) Slurry-mixing electrode. (F) Electrochemical performance comparison of SSLBs assembled with dry-mixing electrodes and slurry-mixing electrodes. Reproduced with permission [48], Copyright 2018, Elsevier Ltd. (G) Schematic illustration of an NMC electrode fabricated by a dry film method. Reproduced with permission [49], Copyright 2019, Elsevier Ltd.

components, especially the binders can hardly tolerate the annealing process. In most cases, it is forced to choose a relatively low annealing temperature and sacrifice some ionic conductivity. To maintain the maximum ionic conductivity of SSE and address the ionic conductivity deterioration caused by the solvent, the dry mixing method has been widely adopted to fabricate the electrode at the lab scale. In most cases, electrode powders can be achieved by mixing the active materials with the SSE using hand-grinding or ball-milling. Following that, relatively high pressure will be applied to press the electrode powders into an electrode pallet. Due to the lack of binder in the electrode, it is only suitable to be evaluated in a model cell instead of a large-size pouch cell. As shown in Fig. 7D, the electrode prepared by the dry-mixing method can eliminate the deterioration effects caused by the binder and solvent and maintain

the intrinsic ionic conductivity of SSEs as well as unblock the Li^+/e^- transport channels blocked by binders (Fig. 7E). As displayed in Fig. 7F, at all active materials (NMC811) contents, the dry-mixing electrodes performed higher active material utilization and CE compared with the slurry-mixing ones (active material loading 20 mg cm^{-2}). It is also noteworthy that the difference is enlarged with the active material content increasing. For instance, with an active material content of 70 wt%, the dry-mixing electrode delivered a discharge capacity of 155 mAh g^{-1} at 0.1C, which is 23 mAh g^{-1} higher than the slurry-mixing electrode. Further increasing the active material content to 85 wt%, which put forward higher requirements on Li^+/e^-, the gap was enlarged to 35 mAh g^{-1} (Fig. 7F) [48]. In this regard, it can conclude that the electrochemical performance of the thick electrode is greatly affected by the solvent and binder. One of the drawbacks for the dry-mixing method is that it is challenging to apply this method for large-size sheet type electrode fabrication and subsequently utilize it in pouch cells. As an alternative, a solvent-free dry film method was developed to fabricate sheet-type electrodes (Fig. 7G). Typically, Polytetrafluoroethylene (PTFE) was chosen as the binder, which can soften at a relatively low temperature (less than 200 °C) and bind the cathode materials together into an electrode. Benefitting from the excellent binding effect of PTFE, the binder content can be reduced to as low as 0.1 wt%, which is considered to be low enough to alleviate its adverse effect on blocking Li^+/e^- transport. Based on this method, a free-standing sheet type NMC electrode with a size greater than 14 cm^2 was demonstrated. Moreover, a $LiNi_{0.9}Mn_{0.05}Co_{0.05}O_2$ electrode with a high areal loading of 6.5 mAh cm^2 was prepared and delivered a high discharge capacity of 203 mAh g^{-1} and a CE of 89% using Li—In as an anode in the voltage window of 1.93—3.63 V (vs. Li—In) at 0.15 mA cm^{-2} [49]. In another case, the dry film approach was adopted to develop a sheet-type $LiNi_{0.9}Mn_{0.05}Co_{0.05}O_2$ and Li_6PS_5Cl composite cathode. A 0.6 Ah prototype ASSLB demonstrated an exceptional volume energy density of 900 Wh L^{-1} with ultralong cycling life of over 1000 cycles at 0.5C [23]. In this regard, during thick electrode design, it is necessary to maximumly reduce the deterioration effect of binder and solvent. The dry film method shows a promising application in large-size sheet type electrode fabrication and subsequently applied in pouch cells.

2.3.4. Enhancement of electronic conductivity

In the above sections, we have highlighted the importance of Li^+ transport towards high-performance thick electrodes and systematically summarized some strategies to improve Li^+ diffusion in the electrode. Besides, electron transport, as another important parameter, also has a big effect on the electrochemical performance of ASSLBs. For instance, for the sulfur cathode, the poor electronic conductivity of 5×10^{-30} S cm^{-1} resulting in poor electrochemical kinetics significantly limits the improvement of rate performance and development of thick electrodes [74,75]. Besides the introduction of conductive additives, the enhancement of sulfur kinetics is another effective strategy to improve the overall electrochemical performance. Compared with sulfur, metal sulfides (MS_x) possess higher electronic conductivity and electrochemical kinetics, which have been chosen as the active materials and demonstrated improved electrochemical performance [19,76,77]. As shown in Fig. 8A, Xu's group synthesized Co_8S_9 nanosheets via a facile solution method and then in-situ grew nano-sized $Li_7P_3S_{11}$ SSE on their surface, which functioned as the composite electrode in ASSLSBs. Attributing to the improved electronic conductivity of Co_8S_9 nanosheets and well-built SSE/active material interface, the assembled ASSLSBs demonstrated a high energy density of 360 Wh kg^{-1} and power density of 3823 W kg^{-1} at 0.13 and 12.73 mA cm^{-2}, respectively [19]. Based on this concept, FeS_x, [78] CuS, [79] and MoS_3, [80,81] have also been reported and shown promising electrochemical performance. Despite their merits in improving electrochemical kinetics, the reduced capacity and lower potential vs. Li^+/Li will no doubt limit the energy density improvement. To alleviate the adverse effect, sulfur was introduced as another component to synthesize the composite electrode ($MS_x + S$) via a facile ball-milling method, where MS_x works as a sulfur host to facilitate the electron transport and improve the electrochemical kinetics of sulfur. In comparison with the single component electrode, either sulfur or MS_x, the composite electrode is more promising by balancing the electrochemical kinetics and theoretical energy density. As a proof of concept, with an active material loading of 1 mg cm^{-2}, the FeS_2+S (the weight ratio of FeS_2 to S is 1/1) electrode delivered a high discharge capacity of 1200 mAh $g_{(FeS2+S)}^{-1}$ at 20 °C (operating current density: 83.5 mA g^{-1}), equaling to an areal capacity of 1.2 mAh cm^{-2}. Further increasing the active material loading to 5 mg cm^{-2}, the areal capacity can be as high as 3.55 mAh cm^{-2}(operating current density: 16.7 mA g^{-1}) [77]. In another case, CuS performed the same functions. With an optimized weight ratio of CuS to S of 1/2, the assembled ASSLSBs delivered a high capacity of 1600 mAh $g_{(CuS+S)}^{-1}$ at 20 mA g^{-1}, where active material loading is 5 mg cm^{-2}, corresponding to a high areal capacity of 8 mAh cm^{-2}. More importantly, the higher density of CuS also leads to an improved volumetric capacity of 3900 mAh $cm_{(CuS+S)}^{-3}$ [76].

Besides the metal sulfides, Se, another element in the VI group, is another good choice due to its higher electronic conductivity (1×10^{-5} S cm^{-1}) [82,83]. Compared with metal sulfides, Se possesses a similar oxidization potential vs. Li^+/Li compared with sulfur and is able to produce SeS_x in any ratio, thus providing the opportunities to tune the theoretical capacity and electronic conductivity. Recently, our group reported high-performance SeS_x cathodes with different Se/S ratios, where the Se element facilitates fast electron transport and enables fast electrochemical reaction kinetics (Fig. 8B). With an optimized Se/S ratio of 1/2 (labeled as SeS_2), the ASSLSBs demonstrated promising electrochemical performance. As displayed in Fig. 8C, with a SeS_2 ultrahigh loading of 15.3 mg cm^{-2}, the assembled SSLSBs delivered a capacity of 824 mAh g^{-1} under a current density of 30 mA g^{-1}, equaling to a high areal capacity of 12.6 mAh cm^{-2} [50].

In the above section, we have summarized some recent progress on enhancing the electronic conductivity of sulfur cathodes via introducing Se element and metal elements. For Li-ion battery cathodes such as LCO and NMC, the facile method to improve the electronic conductivity is to introduce conductive additives. However, the accelerating SSE decomposition under relatively high voltages (typically >4.2) because of high conductive additives hindered their application [84,85]. In most cases, conductive additive-free electrodes have been chosen to alleviate the SSE decomposition [61,86]. At the same time, the limitation in electronic conductivity harms the rate performance. This situation would be even worse in thick electrodes due to the prolonged electron transport distance. Thus, it is still of significance to explore suitable conductive additives to improve the electrochemical performance of thick electrodes. Strauss et al. have investigated the effect of different conductive additives on the electrochemical performance of ASSLBs. Their results suggested that the conductive additives with low surface areas performed a positive effect on improving the rate performance as well as capacity output, while the conductive additives with high surface areas presented a negative effect [87]. A similar positive effect was also proved by Mizuno and his coworkers with a low-surface area vapor grown carbon fibers (VGCF) carbon additive [88]. The phenomenon can be explained by the improved e^- transport capability and limited side reactions within low-surface-area conductive additives

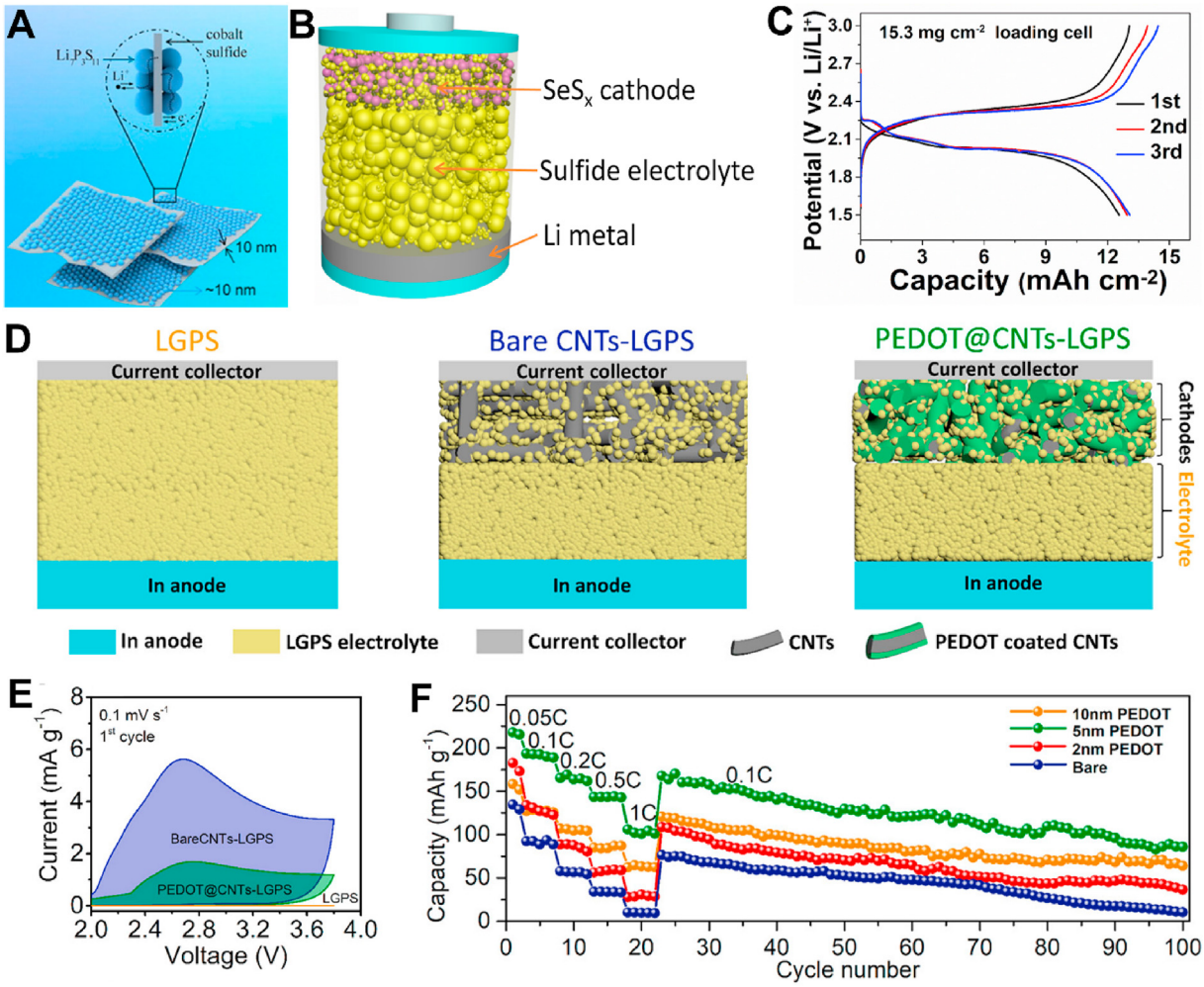

Fig. 8. (A) Schematic diagram of Co_9S_8–$Li_7P_3S_{11}$ nanocomposite. Reproduced with permission from Ref. [19], Copyright 2016, American Chemical Society. (B) Schematic diagram of a Li/SeS_x SSLSB. (C)Cycling stability of an SSLSB assembled with a SeS_2 loading of 15.3 mg cm^{-2} at 30 mA g^{-1}. Reproduced with permission [50], Copyright 2019, Wiley–VCH. (D) Schematic illustration of the designed model cells for SSE decomposition study. (E) CV profiles of the model cells at 0.1 mV s^{-1} during the first cycle. (F) Comparison of SSLBs with unmodified CNTs and PEDOT-modified CNTs in the cathodes. Reproduced with permission [89], Copyright 2020, American Chemical Society.

[88]. In another case, our group designed poly(3,4-ethylenedioxythiophene) (PEDOT) coated carbon nanotubes (CNTs) as semiconductive additives and realized improved electrochemical performance (Fig. 8D). As the cyclic voltammetry (CV) results shown in Fig. 8E, the ASSLBs assembled with PEDOT-modified CNTs showed 0.2 V higher onset potential (2.17 V) and 3.3 times lower peak current density (1.71 mA g^{-1}) compared with unmodified CNTs (1.97 V and 5.63 mA g^{-1}). The higher onset potential and lower peak current prove the positive effect of PEDOT coating on suppressing SSE decomposition. Moreover, as displayed in Fig. 8F, with an optimized PEDOT coating of 5 nm, the assembled ASSLB demonstrates a competitive capacity of over 100 mAh g^{-1} at 1C, which is 10 times greater than that of the cathode with unmodified CNTs [89]. However, the capacity decay was still observed, suggesting the existence of electrolyte decomposition because of high electronic conductivity additives. To eliminate the electrolyte decomposition, it is necessary to further extend the oxidization potential of the SSE in the cathode.

In brief summary, sulfide- and halide- ASSLBs are quite different systems compared with SPE- and oxide-systems, where the design of thick electrodes performs quite differently. Generally, there are four strategies to enhance the electrochemical performance of the thick electrodes. 1) Solution-based interfacial engineering. The liquified and flowable SSE solution can well wet the electrodes as well as create a tri-phase interface via enveloping the electrode materials, which can easier transfer the traditional slurry casting electrode into ASSLBs. More attention should be paid to the annealing process for recovering the ionic conductivity. Choosing a suitable post-treatment temperature, current collector, binder as well as sealing packages are also of significance. 2) Improvement of electrode materials kinetics. The particle size and crystal structure also have a big effect on Li^+ transport during thick electrode fabrication. Generally, single-crystal materials with continuous Li^+ transport pathways, large particle size active materials and small particle size SSEs are preferred. Thus, it is necessary to optimize the cathode materials and SSEs before structural design. 3) Alleviating the deterioration effect of solvent and binder. The binders play an important role in binding the electrode materials and enable the electrode with high flexibility. On the other hand, the existence of non-ionic and non-electronic conductive binders will block the Li^+/e^- transport pathways, leading to low capacity output and large overpotentials. For the solvent, most sulfide- and halide- SSEs are solvent-sensitive, there are some side reactions between solvents and SSEs, resulting in deteriorated ionic conductivity. Even though some SSEs show high recoverability, a high temperature is needed, which causes some difficulty with the binder and sealing packages

as well as electrode materials. Thus, in practical application, it would be much better to avoid involving the solvents and controlling the binder content in a very low range. Taking these requirements into consideration, the dry film method shows a more promising perspective compared with the traditional slurry casting method on large-size sheet-type thick electrodes. 4) Enhancement of electronic conductivity. Besides Li^+ transport, the electronic conductivity of the thick electrode is equally important. Simply by introducing the carbon additive into the electrode, there will be a serious SSE decomposition because of improved electronic conductivity. It is necessary to balance the positive effect of electronic conductivity and the adverse effect of SSE decomposition. Moreover, the exploration of new SSEs with higher oxidization potentials is urgently required to alleviate the SSE decomposition under high voltages. Besides the use of conductive additives, the improvement of the intrinsic electronic conductivity of active materials is also helpful for thicker electrode building.

2.4. Thick electrode-based pouch cells

The target of the thick electrode is to be used in practical pouch cells and supply energy to portable electronic devices and EVs. Thus, it is of significance to develop reliable large-size thick electrodes and evaluate their performance in the pouch cells, which is considered to be closer to industry application [90,91]. Beyond fundamental studies using coin cells or model cells, some thick electrode-based pouch cells have been reported and demonstrated promising electrochemical performance. As shown in Fig. 9A, Zaghib's group reported a 3.8 cm^2 Li-LFP ASSLB pouch cell, where a 92 μm LFP and a 46 μm Li foil functioned as the cathode and anode, respectively. The pouch cell demonstrated 80% capacity retention with over 1400 cycles at C/3 [18]. Besides, the slurry casting method was applied by Takeuchi's and Jung's groups to fabricate sheet-type sulfide SSE-based graphite-NMC pouch cells, where NMC111 and NMC622 were chosen as the active materials, respectively. The areal capacities in Takeuchi's and Jung's cases are over 1.5 and 2 mAh cm^{-2}, resulting in high energy densities of 155 Wh kg^{-1} (pouch cell size: 22 × 22 mm^2) and 184 Wh kg^{-1} (pouch cell size: 80 × 60 mm^2) at the cell level [48,51]. In another study, Aihara et al. reported a 1 Ah class graphite-$LiNi_{0.8}Co_{0.15}Al_{0.05}O_2$ (NCA) pouch cell by stacking the single cells (Fig. 9B~C) [52]. It should be mentioned that the pouch cells reported in the sulfide system are mostly using graphite as the anode, where no Li dendrite issue is involved. Nevertheless, the energy density improvement was limited by the low capacity of the graphite anode. To avoid using graphite that would reduce the energy density, researchers from Samsung Electronics Co., Ltd developed a Li-free Ag—C anode for ASSLB pouch cells. Accordingly, the Ag—C composite layer facilitated smooth Li deposition and a dense Li layer was observed to be repeated formation and dissolve between the Ag—C composite and anode current collector. Additionally, at the early stage of the charging process, Ag nanoparticles were alloyed and formed Li—Ag alloy, but a significant fraction of Ag was observed to migrate towards the current collector and assist the uniform Li deposition. As a consequence, a 6.7 × 11.2 cm^2 Li— $LiNi_{0.90}Mn_{0.05}Co_{0.05}O_2$ ASSLB pouch cell with a high capacity of 0.6 Ah (Fig. 9D) presented a high energy density (>900 Wh L^{-1}), high rate performance of over 2C (Fig. 9E) and long cycling life of 1000 cycles [23].

Beyond Li-ion SSLBs, SSLSBs with higher theoretical energy density using thick electrodes have already been reported. Wachsman and his coworkers reported an “all-in-one” SSLSB pouch cell based on a porous-dense-porous garnet architecture, where the dense layer acted as the SSE and porous layers functioned as the hosts for Li and sulfur accommodation (Fig. 9F). With a high sulfur loading of 5.3 mg cm^{-2}, the SSLSB pouch cell delivered a high reversible capacity of over 1200 mAh g^{-1} within 8 cycles at 0.1C, equaling to a high energy density of 195 Wh kg^{-1} based on total cell mass (Fig. 9G) [40]. In another case, Zhang's group reported a 33 × 33 mm^2 sulfide-SSE-based SSLSB pouch cell based on the slurry coating electrode. The cell using 1.8 mg cm^{-2} sulfur-loaded cathode demonstrated a high areal capacity of 2.3 mAh cm^{-2} at 0.01C [92]. The aforementioned achievements indicate promising prototypes for high-energy-density ASSLBs.

3. Conclusion and perspective

With the increasing development of EVs and portable electronic devices, the pursuit of high safety and high-energy-density energy storage devices beyond state-of-the-art Li-ion batteries accelerated the development of ASSLBs. Compared with thin electrodes, thick electrodes have recently received more attention due to their possibility to further improve the energy density by reducing the ratio of the inactive components in the ASSLBs. Nevertheless, their practical application is highly restricted by the deteriorated reaction kinetics because of prolonged or blocked Li^+/e^- transport.This review has summarized the potential strategies to realize high-performance thick electrodes with fast electrochemical kinetics, high active materials utilization as well as improved rate performance (Fig. 10). Even though not all of the mentioned strategies have demonstrated their application in thick electrodes, the improved electrochemical performance (rate performance, high capacity output) provides some clues. Generally speaking, in polymer and oxide- SSEs, one effective strategy is to build fast Li^+ transport channels in the cathodes via reducing the tortuosity, especially for the vertically aligned structures [34,38]. Another promising strategy for the oxide-SSE-based thick electrode is addressing the interfacial issues related to the solid-solid contact between the electronic conductor, ionic conductor and active materials. For sulfide- and halide-SSE-based systems, most ASSLBs are evaluated by model cells and high pressure is applied, the design of a 3D structure for facilitating Li^+ transport is rarely reported. Instead, most of the efforts are focused on addressing the interfacial issues, enhancing the electrochemical kinetics of active materials, reducing the deterioration effect of binders and solvents as well as improving the electronic conductivity. Based on the aforementioned solutions, great progress has been made. Some pouch cells have demonstrated a high energy density of over 200 Wh kg^{-1} at the cell level. Although promising results have been achieved using thick electrodes in ASSLBs, there are still significant challenges (volume change, Li dendrite suppression, scalability, etc.) that need to be overcome. The potential directions and outlook for ASSLBs can be summarized as follows:

1) Large-size sheet type thick electrode fabrication.

It is of significance to realize the large-size sheet type thick electrode fabrication for realistic industrial scalability. In polymer systems, it is easy to transfer the traditional slurry casting electrodes to be used in ASSLBs via replacing the binder with the SPEs for facilitating Li^+ transport. Similarly, extrusion will be another good method for large-size SPE-based electrode fabrication [93]. For sulfide and halide electrodes, the slurry casting method is also a good choice. However, the side reactions between SSE and solvent should be carefully considered during electrode design. To avoid the use of solvents, the dry film method seems more promising, which can maintain the intrinsic properties of the binders, SSEs and active materials. More importantly, the binder content can be reduced to as low as 0.1 wt% [49]. It significantly reduces the deterioration effect of the binder on blocking Li^+/e^- transport. For oxide SSE-base electrodes, the most widely adopted method is tape

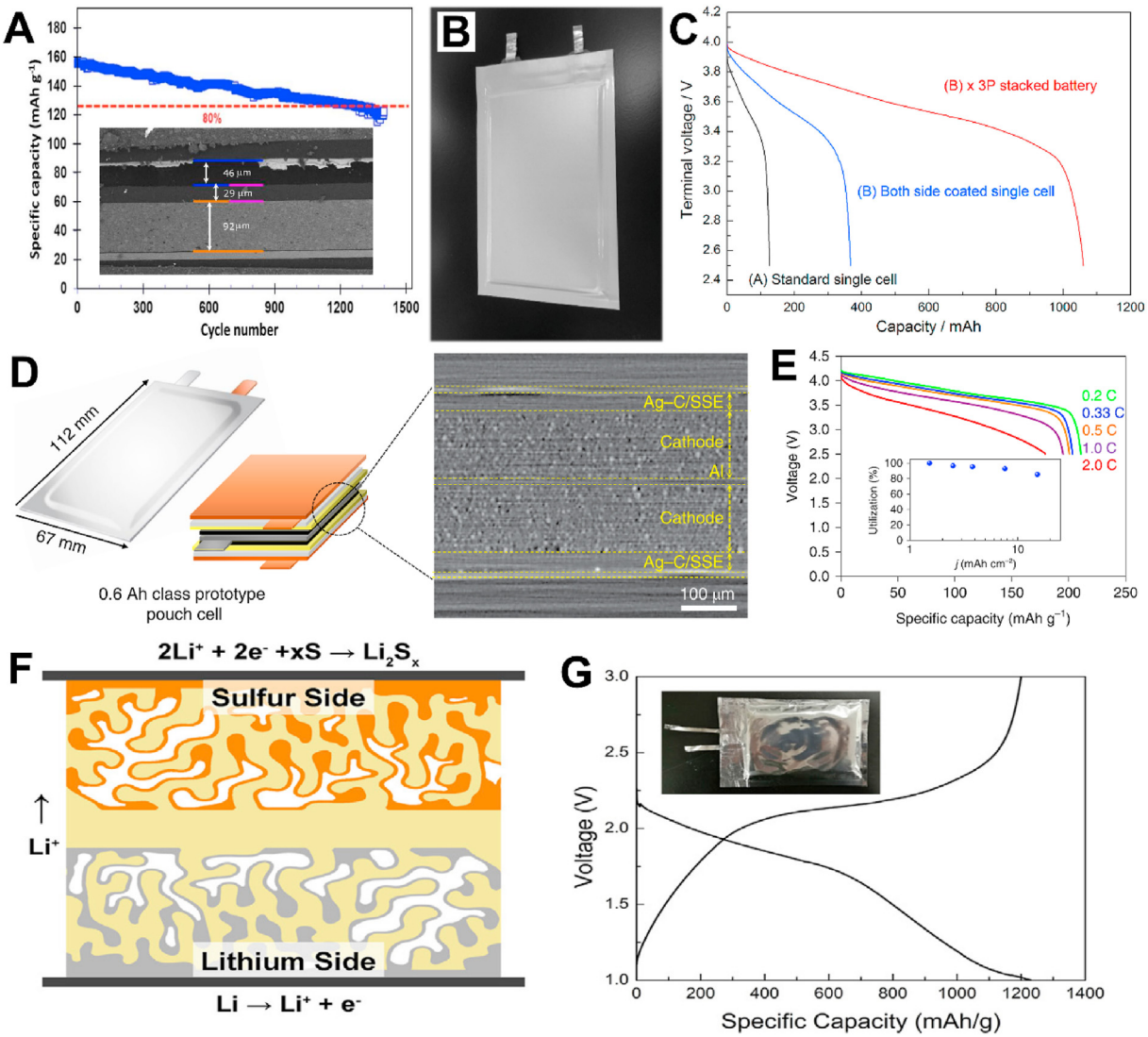

Fig. 9. (A) Cycling stability of a Li-LFP SSLB pouch cell at C/3, insert is the cross-sectional SEM image of the cell. Reproduced with permission from Ref. [18]. Copyright (2015) American Chemical Society. (B) Optical image and (C) discharge profile of 1 Ah stacked graphite- $LiNi_{0.8}Co_{0.15}Al_{0.05}O_2$ pouch cell. Reproduced with permission from Ref. [52]. Copyright (2014) Elsevier Ltd. (D) Schematic illustration and X-ray computed tomography and (E) rate performance of a 0.6 Ah Li–$LiNi_{0.90}Mn_{0.05}Co_{0.05}O_2$ SSLB pouch cell. Reproduced with permission from Ref. [23]. Copyright 2020, Nature Publishing Group. (F) Schematic illustration of an "all-in-one" SSLSB and (G) related optical image and charging-discharging profiles. Reproduced with permission from Ref. [40]. Copyright (2019) Elsevier Ltd.

casting with a post-annealing process to reduce the interfacial resistance. Nevertheless, its industry-scale production remains challenging.

2) High-performance electrolyte

The electrochemical performance of SSLBs is largely determined by the nature of SSEs. Higher ionic conductivity in SSEs always means faster Li^+ transport capability in the electrodes. Thus, it is of significance to develop high-ionic conductivity SSEs, and its positive effect has already been demonstrated in thick electrode design [94,95]. Aside from looking for SSEs with high ionic conductivity, exploring SSEs with wider electrochemical stability windows is another important direction. Machine learning (ML) would give some help for designing high-performance electrolytes [96]. Chen's group discovered 16 new SSEs with RT conductivities higher than 10^{-4} S cm^{-1} by using ML [97]. In another case, Sendek's results suggest that halide-based SSEs and doped sulfide SSEs were shown to be more promising due to their better electrochemical stability and enhanced ionic conductivity [98]. Besides the chemical properties of the SSE, the development of thin electrolyte layers is also of significance. According to the simulations, a thin SSE with a thickness of less than 50 μm is essential to achieve a high energy density of over 300 Wh kg^{-1} [28,29,99]. Similar to electrode fabrication, slurry casting and extrusion methods are suitable for thin SPEs fabrication. Dry film/slurry casting and tape casting techniques are more appreciated for sulfur-/halide- and oxide-SSEs fabrication [99,100]. During the design of thin SSEs, the mechanical properties, scalability, flexibility, ionic conductivity, as well as its stability against anode and cathode, should be taken into consideration.

(3) High-performance anode

Besides the improved safety, one of the biggest merits of ASSLBs beyond traditional Li-ion batteries is their potential for high energy

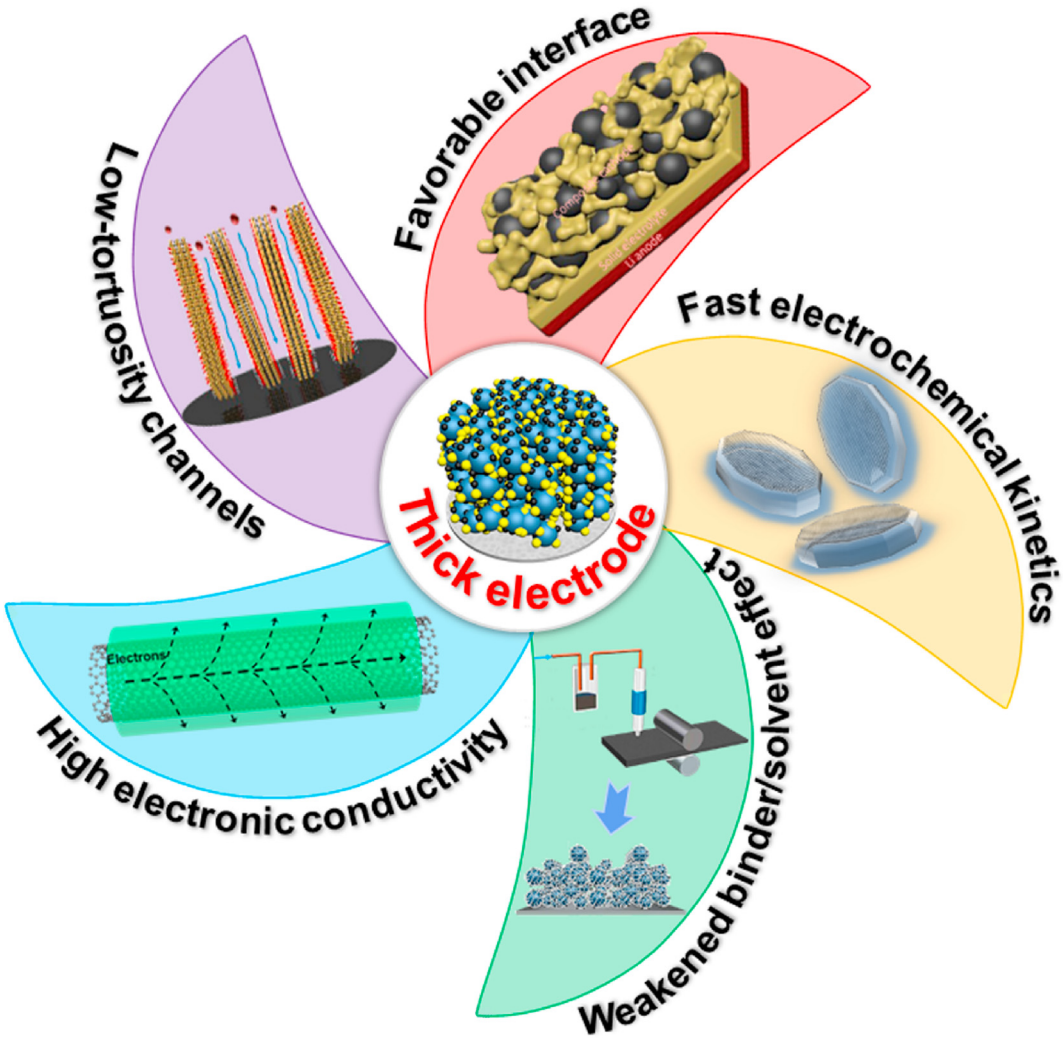

Fig. 10. Summary of potential strategies to improve the electrochemical performance of thick electrodes. Reproduced with permission [116], Copyright 2018, Nature Publishing Group. Reproduced with permission [117], Copyright 2021, Wiley-VCH. Reproduced with permission [118], Copyright 2016, Nature Publishing Group. Reproduced with permission [89], Copyright 2020, American Chemical Society.

density using a Li anode. Nevertheless, using Li metal as an anode in ASSLBs remains challenging due to the Li dendrite growth, especially for the thick electrodes with high capacities, which hinders its application in ASSLBs, [22,101] In most cases, graphite and Li-metal alloys (or In metal) are chosen as the anode materials to inhibit Li dendrite growth and has been proven to be effective in prolonging the cycling life of SSLBs [47,48,51]. The main drawbacks of the two anode materials are that the low theoretical capacity of graphite (372 mAh g^{-1}) and higher potential of Li-metal alloys vs. Li/Li^+ (eg. Li—In: ~0.6 V) will limit the improvement of energy density in practical application. Based on potential and theoretical capacity consideration, Li—Mg alloy with a lower potential vs Li^+/Li (0.0325 V) and high capacity over 2000 mAh g^{-1} is one promising direction [102]. Using thin graphite or Li-metal alloys as Li anode protection layers to suppress Li dendrite growth as well as maintaining the Li capacity and potential is another direction [103,104]. Recently, a high-performance Li-free anode has also demonstrated its potential application in high-energy-density cell configurations [23,105]. In practical application, to ensure high CE and high utilization of reversible Li, replenishing a small amount of lithium at the anode side will be reasonable. Additionally, the exploration of effective Li protection methods is critical for achieving high-performance thick electrode-based ASSLBs [75,101,106,107].

(4) Volume change

According to previous reports, the volume changes are from approximately −7% to +2% for Ni- (NMC811) and Co-rich (LCO) cathode materials [108]. For sulfur, the volume change is roughly 80% [109,110]. Besides, the thickness change at electroactive Li at the anode side is also around 20 μm in 4 mAh cm^{-2} ASSLBs. The huge volume change will result in the worsening contact between SSE and electrode materials as well as mechanical damage of the SSE layer, leading to increased interfacial resistance and capacity decay. To address the issue, several potential solutions are provided. (1) as a widely accepted strategy used in Li—S batteries, reserving the void space for volume change will be a promising direction; (2) externally applied pressure has demonstrated its positive effect on enhancing the cycling stability and capacity output, which has the potential to be shifted to pouch cells [111,112]; (3) as we mentioned above, the NMC cathodes show opposite volume expansion trends with LCO electrodes. The combination of the LCO and NMC cathodes or adjustment of the Mn/Co ratio is helpful to realize a zero-strain cathode with less overall

volume fluctuation [108,113]. (4) single-crystal cathode materials performed uniform volume change of the whole primary particle, enabling intimate contact of cathode materials with electronic/ionic conductors, which would be another good choice [70–72]. Lastly, it is also worth investigating flexible, pressure self-adaptable binders to alleviate the volume change [114].

To realize high energy density, it is necessary to couple the thick electrodes with thin SSEs and thin Li anode [115]. That means more work should be focused on different parts to accelerate the industrialization of ASSLBs from both fundamental studies and engineering design.

Declaration of competing interest

The authors declare no conflicts of interest.

Acknowledgments

This work was partly supported by Natural Sciences and Engineering Research Council of Canada (NSERC), Canada Research Chair Program (CRC), Canada Foundation for Innovation (CFI), Ontario Research Fund, China Automotive Battery Research Institute Co., Ltd, Glabat Solid-State Battery Inc. and University of Western Ontario. Xiaofei Yang appreciates the support of the MITACS Elevate postdoctoral program.

References

[1] Tarascon J-M, Armand M. Nature 2001;414:359–67.
[2] Armand M, Tarascon J-M. Nature 2008;451:652–7.
[3] Cheng XB, Zhang R, Zhao CZ, Zhang Q. Chem Rev 2017;117:10403–73.
[4] Lu J, Chen Z, Pan F, Cui Y, Amine K. Electrochem Energy Rev 2018;1:35–53.
[5] Chen R, Li Q, Yu X, Chen L, Li H. Chem Rev 2019;120:6820–77.
[6] Liu J, Bao Z, Cui Y, Dufek EJ, Goodenough JB, Khalifah P, Li Q, Liaw BY, Liu P, Manthiram A, Meng YS, Subramanian VR, Toney MF, Viswanathan VV, Whittingham MS, Xiao J, Xu W, Yang J, Yang X-Q, Zhang J-G. Nat Energy 2019;4:180–6.
[7] Zhao W, Yi J, He P, Zhou H. Electrochem Energy Rev 2019;2:574–605.
[8] Yan Y, Ju J, Dong S, Wang Y, Huang L, Cui L, Jiang F, Wang Q, Zhang Y, Cui G. Adv Sci 2021;8:2003887.
[9] Wang Y, Ju J, Dong S, Yan Y, Jiang F, Cui L, Wang Q, Han X, Cui G. Adv Funct Mater 2021;31:2101523.
[10] Manthiram A, Yu X, Wang S. Nat Rev Mater 2017;2:16103.
[11] Chu Y, Shen Y, Guo F, Zhao X, Dong Q, Zhang Q, Li W, Chen H, Luo Z, Chen L. Electrochem Energy Rev 2019;3:187–219.
[12] Wu J, Shen L, Zhang Z, Liu G, Wang Z, Zhou D, Wan H, Xu X, Yao X. Electrochem Energy Rev 2020;4:101–35.
[13] Kamaya N, Homma K, Yamakawa Y, Hirayama M, Kanno R, Yonemura M, Kamiyama T, Kato Y, Hama S, Kawamoto K, Mitsui A. Nat Mater 2011;10:682–6.
[14] Kato Y, Hori S, Saito T, Suzuki K, Hirayama M, Mitsui A, Yonemura M, Iba H, Kanno R. Nat Energy 2016;1:16030.
[15] Li X, Liang J, Luo J, Norouzi Banis M, Wang C, Li W, Deng S, Yu C, Zhao F, Hu Y, Sham T-K, Zhang L, Zhao S, Lu S, Huang H, Li R, Adair KR, Sun X. Energy Environ Sci 2019;12:2665–71.
[16] Li X, Liang J, Chen N, Luo J, Adair KR, Wang C, Banis MN, Sham TK, Zhang L, Zhao S, Lu S, Huang H, Li R, Sun X. Angew Chem Int Ed 2019;58:16427–32.
[17] Han Q, Li X, Shi X, Zhang H, Song D, Ding F, Zhang L. J Mater Chem A 2019;7:3895–902.
[18] Hovington P, Lagace M, Guerfi A, Bouchard P, Mauger A, Julien CM, Armand M, Zaghib K. Nano Lett 2015;15:2671–8.
[19] Yao X, Liu D, Wang C, Long P, Peng G, Hu YS, Li H, Chen L, Xu X. Nano Lett 2016;16:7148–54.
[20] Yan H, Wang H, Wang D, Li X, Gong Z, Yang Y. Nano Lett 2019;19:3280–7.
[21] Gao X, Yang X, Adair K, Liang J, Sun Q, Zhao Y, Li R, Sham TK, Sun X. Adv Funct Mater 2020;30:2005357.
[22] Yang X, Gao X, Mukherjee S, Doyle-Davis K, Fu J, Li W, Sun Q, Zhao F, Jiang M, Hu Y, Huang H, Zhang L, Lu S, Li R, Sham TK, Singh CV, Sun X. Adv Energy Mater 2020;10:2001191.
[23] Lee Y-G, Fujiki S, Jung C, Suzuki N, Yashiro N, Omoda R, Ko D-S, Shiratsuchi T, Sugimoto T, Ryu S, Ku JH, Watanabe T, Park Y, Aihara Y, Im D, Han IT. Nat Energy 2020;5:299–308.
[24] https://oxisenergy.com/https-oxisenergy-com-wp-content-uploads-2020-01-500-and-600-whkg-pressor-pdf/.
[25] Randau S, Weber DA, Kötz O, Koerver R, Braun P, Weber A, Ivers-Tiffée E, Adermann T, Kulisch J, Zeier WG, Richter FH, Janek J. Nat Energy 2020;5:259–70.
[26] Kato Y, Shiotani S, Morita K, Suzuki K, Hirayama M, Kanno R. J Phys Chem Lett 2018;9:607–13.
[27] Liu L, Xu J, Wang S, Wu F, Li H, Chen L. eTransportation 2019;1:100010.
[28] Yang X, Adair KR, Gao X, Sun X. Energy Environ Sci 2021;14:643–71.
[29] Wu J, Yuan L, Zhang W, Li Z, Xie X, Huang Y. Energy Environ Sci 2021;14:12–36.
[30] Kuang Y, Chen C, Kirsch D, Hu L. Adv Energy Mater 2019;9:1901457.
[31] Zhang B, Chen L, Hu J, Liu Y, Liu Y, Feng Q, Zhu G, Fan L-Z. J Power Sources 2019;442:227230.
[32] Lin D, Yuen PY, Liu Y, Liu W, Liu N, Dauskardt RH, Cui Y. Adv Mater 2018;30:e1802661.
[33] Zhao Q, Liu X, Stalin S, Khan K, Archer LA. Nat Energy 2019;4:365–73.
[34] Yang X, Sun Q, Zhao C, Gao X, Adair KR, Liu Y, Luo J, Lin X, Liang J, Huang H, Zhang L, Yang R, Lu S, Li R, Sun X. Nano Energy 2019;61:567–75.
[35] Fu K, Gong Y, Hitz GT, McOwen DW, Li Y, Xu S, Wen Y, Zhang L, Wang C, Pastel G, Dai J, Liu B, Xie H, Yao Y, Wachsman ED, Hu L. Energy Environ Sci 2017;10:1568–75.
[36] Gong Y, Fu K, Xu S, Dai J, Hamann TR, Zhang L, Hitz GT, Fu Z, Ma Z, McOwen DW, Han X, Hu L, Wachsman ED. Mater Today 2018;21:594–601.
[37] Zhang Z, Chen S, Yao X, Cui P, Duan J, Luo W, Huang Y, Xu X. Energy Storage Mater 2020;24:714–8.
[38] Shen H, Yi E, Amores M, Cheng L, Tamura N, Parkinson DY, Chen G, Chen K, Doeff M. J Mater Chem A 2019;7:20861–70.
[39] Xu S, McOwen DW, Zhang L, Hitz GT, Wang C, Ma Z, Chen C, Luo W, Dai J, Kuang Y, Hitz EM, Fu K, Gong Y, Wachsman ED, Hu L. Energy Storage Mater 2018;15:458–64.
[40] Hitz GT, McOwen DW, Zhang L, Ma Z, Fu Z, Wen Y, Gong Y, Dai J, Hamann TR, Hu L, Wachsman ED. Mater Today 2019;22:50–7.
[41] Yi E, Shen H, Heywood S, Alvarado J, Parkinson DY, Chen G, Sofie SW, Doeff MM. ACS Appl Energy Mater 2020;3:170–5.
[42] Li F, Li J, Zhu F, Liu T, Xu B, Kim T-H, Kramer MJ, Ma C, Zhou L, Nan C-W. Matter 2019;1:1001–16.
[43] Han F, Yue J, Fan X, Gao T, Luo C, Ma Z, Suo L, Wang C. Nano Lett 2016;16:4521–7.
[44] Kim MJ, Park JW, Kim BG, Lee YJ, Ha YC, Lee SM, Baeg KJ. Sci Rep 2020;10:11923.
[45] Kim DH, Lee Y-H, Song YB, Kwak H, Lee S-Y, Jung YS. ACS Energy Lett 2020;5:718–27.
[46] Wang C, Liang J, Jiang M, Li X, Mukherjee S, Adair K, Zheng M, Zhao Y, Zhao F, Zhang S, Li R, Huang H, Zhao S, Zhang L, Lu S, Singh CV, Sun X. Nano Energy 2020;76:105015.
[47] Yamamoto M, Terauchi Y, Sakuda A, Takahashi M. Sci Rep 2018;8:1212.
[48] Nam YJ, Oh DY, Jung SH, Jung YS. J Power Sources 2018;375:93–101.
[49] Hippauf F, Schumm B, Doerfler S, Althues H, Fujiki S, Shiratsuchi T, Tsujimura T, Aihara Y, Kaskel S. Energy Storage Mater 2019;21:390–8.
[50] Li X, Liang J, Luo J, Wang C, Li X, Sun Q, Li R, Zhang L, Yang R, Lu S, Huang H, Sun X. Adv Mater 2019;31:e1808100.
[51] Sakuda A, Kuratani K, Yamamoto M, Takahashi M, Takeuchi T, Kobayashi H. J Electrochem Soc 2017;164:A2474–8.
[52] Ito S, Fujiki S, Yamada T, Aihara Y, Park Y, Kim TY, Baek S-W, Lee J-M, Doo S, Machida N. J Power Sources 2014;248:943–50.
[53] Duan H, Yin Y-X, Zeng X-X, Li J-Y, Shi J-L, Shi Y, Wen R, Guo Y-G, Wan L-J. Energy Storage Mater 2018;10:85–91.
[54] Wang C, Ping W, Bai Q, Cui H, Hensleigh R, Wang R, Brozena AH, Xu Z, Dai J, Pei Y, Zheng C, Pastel G, Gao J, Wang X, Wang H, Zhao J-C, Yang B, Zheng XR, Luo J, Mo Y, Dunn B, Hu L. Science 2020;368:521–6.
[55] Wang C, Fu K, Kammampata SP, McOwen DW, Samson AJ, Zhang L, Hitz GT, Nolan AM, Wachsman ED, Mo Y, Thangadurai V, Hu L. Chem Rev 2020;120:4257–300.
[56] Huo H, Luo J, Thangadurai V, Guo X, Nan C-W, Sun X. ACS Energy Lett 2019;5:252–62.
[57] Han F, Yue J, Chen C, Zhao N, Fan X, Ma Z, Gao T, Wang F, Guo X, Wang C. Joule 2018;2:497–508.
[58] Yang Y-N, Li Y-X, Li Y-Q, Zhang T. Nat Commun 2020;11:5519.
[59] Zhong G, Wang C, Wang R, Ping W, Xu S, Qiao H, Cui M, Wang X, Zhou Y, Kline DJ, Zachariah MR, Hu L. Energy Storage Mater 2020;30:385–91.
[60] Wang R, Dong Q, Wang C, Hong M, Gao J, Xie H, Guo M, Ping W, Wang X, He S, Luo J, Hu L. Adv Mater 2021;33:e2100726.
[61] Wang C, Liang J, Hwang S, Li X, Zhao Y, Adair K, Zhao C, Li X, Deng S, Lin X, Yang X, Li R, Huang H, Zhang L, Lu S, Su D, Sun X. Nano Energy 2020;72:104686.
[62] Li X, Ren Z, Norouzi Banis M, Deng S, Zhao Y, Sun Q, Wang C, Yang X, Li W, Liang J, Li X, Sun Y, Adair K, Li R, Hu Y, Sham T-K, Huang H, Zhang L, Lu S, Luo J, Sun X. ACS Energy Lett 2019;4:2480–8.
[63] Rosero-Navarro NC, Miura A, Tadanaga K. JSol-Gel Sci Technol 2018;89:303–9.
[64] Wang Y, Lu D, Bowden M, El Khoury PZ, Han KS, Deng ZD, Xiao J, Zhang J-G, Liu J. Chem Mater 2018;30:990–7.
[65] Kim DH, Lee HA, Song YB, Park JW, Lee S-M, Jung YS. J Power Sources 2019;426:143–50.
[66] Li X, Liang J, Adair KR, Li J, Li W, Zhao F, Hu Y, Sham TK, Zhang L, Zhao S, Lu S, Huang H, Li R, Chen N, Sun X. Nano Lett 2020;20:4384–92.
[67] Li W, Liang J, Li M, Adair KR, Li X, Hu Y, Xiao Q, Feng R, Li R, Zhang L, Lu S, Huang H, Zhao S, Sham T-K, Sun X. Chem Mater 2020;32:7019–27.

[68] Wang S, Bai Q, Nolan AM, Liu Y, Gong S, Sun Q, Mo Y. Angew Chem Int Ed 2019;58:8039–43.
[69] Shi T, Tu Q, Tian Y, Xiao Y, Miara LJ, Kononova O, Ceder G. Adv Energy Mater 2020;10:1902881.
[70] Liu X, Zheng B, Zhao J, Zhao W, Liang Z, Su Y, Xie C, Zhou K, Xiang Y, Zhu J, Wang H, Zhong G, Gong Z, Huang J, Yang Y. Adv Energy Mater 2021;11:2003583.
[71] Han Y, Jung SH, Kwak H, Jun S, Kwak HH, Lee JH, Hong ST, Jung YS. Adv Energy Mater 2021:2100126.
[72] Wang C, Yu R, Hwang S, Liang J, Li X, Zhao C, Sun Y, Wang J, Holmes N, Li R, Huang H, Zhao S, Zhang L, Lu S, Su D, Sun X. Energy Storage Mater 2020;30:98–103.
[73] Zhang J, Zhong H, Zheng C, Xia Y, Liang C, Huang H, Gan Y, Tao X, Zhang W. J Power Sources 2018;391:73–9.
[74] Yang X, Li X, Adair K, Zhang H, Sun X. Electrochem Energy Rev 2018;1:239–93.
[75] Yang X, Luo J, Sun X. Chem Soc Rev 2020;49:2140–95.
[76] Hosseini SM, Varzi A, Ito S, Aihara Y, Passerini S. Energy Storage Mater 2020;27:61–8.
[77] Ulissi U, Ito S, Hosseini SM, Varzi A, Aihara Y, Passerini S. Adv Energy Mater 2018;8:1801462.
[78] Pan M, Hakari T, Sakuda A, Hayashi A, Suginaka Y, Mori S, Tatsumisago M. Electrochemistry 2018;86:175–8.
[79] Machida N, Kobayashi K, Nishikawa Y, Shigematsu T. Solid State Ionics 2004;175:247–50.
[80] Matsuyama T, Deguchi M, Hayashi A, Tatsumisago M, Ozaki T, Togawa Y, Mori S. Electrochemistry 2015;83:889–93.
[81] Zhang Q, Ding Z, Liu G, Wan H, Mwizerwa JP, Wu J, Yao X. Energy Storage Mater 2019;13:168–80.
[82] Li X, Liang J, Li X, Wang C, Luo J, Li R, Sun X. Energy Environ Sci 2018;11:2828–32.
[83] Gao X, Yang X, Wang S, Sun Q, Zhao C, Li X, Liang J, Zheng M, Zhao Y, Wang J, Li M, Li R, Sham T-K, Sun X. J Mater Chem A 2020;8:278–86.
[84] Zhang W, Leichtweiss T, Culver SP, Koerver R, Das D, Weber DA, Zeier WG, Janek J. ACS Appl Mater Interfaces 2017;9:35888–96.
[85] Yoon K, Kim JJ, Seong WM, Lee MH, Kang K. Sci Rep 2018;8:8066.
[86] Zhao F, Liang J, Yu C, Sun Q, Li X, Adair K, Wang C, Zhao Y, Zhang S, Li W, Deng S, Li R, Huang Y, Huang H, Zhang L, Zhao S, Lu S, Sun X. Adv Energy Mater 2020;10:1903422.
[87] Strauss F, Stepien D, Maibach J, Pfaffmann L, Indris S, Hartmann P, Brezesinski T. RSC Adv 2020;10:1114–9.
[88] Mizuno F, Hayashi A, Tadanaga K, Tatsumisago M. J Electrochem Soc 2005;152:A1499.
[89] Deng S, Sun Y, Li X, Ren Z, Liang J, Doyle-Davis K, Liang J, Li W, Norouzi Banis M, Sun Q, Li R, Hu Y, Huang H, Zhang L, Lu S, Luo J, Sun X. ACS Energy Lett 2020;5:1243–51.
[90] Yang X, Jiang M, Gao X, Bao D, Sun Q, Holmes N, Duan H, Mukherjee S, Adair K, Zhao C, liang j, Li W, Li J, Liu Y, Huang H, Zhang L, Lu S, Lu Q, Li R, Singh CV, Sun X. Energy Environ Sci 2020;13:1318–25.
[91] Li X, Liang J, Yang X, Adair KR, Wang C, Zhao F, Sun X. Energy Environ Sci 2020;13:1429–61.
[92] Yuan H, Nan H-X, Zhao C-Z, Zhu G-L, Lu Y, Cheng X-B, Liu Q-B, He C-X, Huang J-Q, Zhang Q. Batteries & Supercaps 2020;3:596–603.
[93] Xie H, Bao Y, Cheng J, Wang C, Hitz EM, Yang C, Liang Z, Zhou Y, He S, Li T, Hu L. ACS Energy Lett 2019;4:2668–74.
[94] Kraft MA, Ohno S, Zinkevich T, Koerver R, Culver SP, Fuchs T, Senyshyn A, Indris S, Morgan BJ, Zeier WG. J Am Chem Soc 2018;140:16330–9.
[95] Kim S, Oguchi H, Toyama N, Sato T, Takagi S, Otomo T, Arunkumar D, Kuwata N, Kawamura J, Orimo SI. Nat Commun 2019;10:1081.
[96] Guo H, Wang Q, Stuke A, Urban A, Artrith N. Front Energy Res 2021;9.
[97] Zhang Y, He X, Chen Z, Bai Q, Nolan AM, Roberts CA, Banerjee D, Matsunaga T, Mo Y, Ling C. Nat Commun 2019;10:5260.
[98] Sendek AD, Cheon G, Pasta M, Reed EJ. J Phys Chem C 2020;124:8067–79.
[99] Zhang Z, Wu L, Zhou D, Weng W, Yao X. Nano Lett 2021;21:5233–9.
[100] Jiang T, He P, Wang G, Shen Y, Nan CW, Fan LZ. Adv Energy Mater 2020;10:1903376.
[101] Cao D, Sun X, Li Q, Natan A, Xiang P, Zhu H. Matter 2020;3:57–94.
[102] Obrovac MN, Chevrier VL. Chem Rev 2014;114:11444–502.
[103] Su Y, Ye L, Fitzhugh W, Wang Y, Gil-González E, Kim I, Li X. Energy Environ Sci 2020;13:908–16.
[104] Liang X, Pang Q, Kochetkov IR, Sempere MS, Huang H, Sun X, Nazar LF. Nat Energy 2017;2:17119.
[105] Wang MJ, Carmona E, Gupta A, Albertus P, Sakamoto J. Nat Commun 2020;11:5201.
[106] Yang X, Sun Q, Zhao C, Gao X, Adair K, Zhao Y, Luo J, Lin X, Liang J, Huang H, Zhang L, Lu S, Li R, Sun X. Energy Storage Mater 2019;22:194–9.
[107] Yang X, Gao X, Zhao C, Sun Q, Zhao Y, Adair K, Luo J, Lin X, Liang J, Huang H, Zhang L, Lu S, Li R, Sun X. Energy Storage Mater 2020;27:198–204.
[108] Strauss F, de Biasi L, Kim AY, Hertle J, Schweidler S, Janek J, Hartmann P, Brezesinski T. ACS Mater Lett 2019;2:84–8.
[109] Yang X, Chen Y, Wang M, Zhang H, Li X, Zhang H. Adv Funct Mater 2016;26:8427–34.
[110] Yang X, Gao X, Sun Q, Jand SP, Yu Y, Zhao Y, Li X, Adair K, Kuo LY, Rohrer J, Liang J, Lin X, Banis MN, Hu Y, Zhang H, Li X, Li R, Zhang H, Kaghazchi P, Sham TK, Sun X. Adv Mater 2019;31:e1901220.
[111] Zhang W, Schröder D, Arlt T, Manke I, Koerver R, Pinedo R, Weber DA, Sann J, Zeier WG, Janek J. J Mater Chem A 2017;5:9929–36.
[112] Li WJ, Hirayama M, Suzuki K, Kanno R. Mater Trans 2016;57:549–52.
[113] Koerver R, Zhang W, de Biasi L, Schweidler S, Kondrakov AO, Kolling S, Brezesinski T, Hartmann P, Zeier WG, Janek J. Energy Environ Sci 2018;11:2142–58.
[114] Shi P, Zhang XQ, Shen X, Li BQ, Zhang R, Hou LP, Zhang Q. Adv Funct Mater 2020:2004189.
[115] Cao D, Zhao Y, Sun X, Natan A, Wang Y, Xiang P, Wang W, Zhu H. ACS Energy Lett 2020;5:3468–89.
[116] Xia Y, Mathis TS, Zhao MQ, Anasori B, Dang A, Zhou Z, Cho H, Gogotsi Y, Yang S. Nature 2018;557:409–12.
[117] Kim KJ, Balaish M, Wadaguchi M, Kong L, Rupp JLM. Adv Energy Mater 2020;11:2002689.
[118] Ludwig B, Zheng Z, Shou W, Wang Y, Pan H. Sci Rep 2016;6:23150.